

Tracer model-based quantitative separation of precipitation and permafrost waters used for evapotranspiration in a boreal forest

Hotaek Park¹, Masahiro Tanoue², Kimpei Ichiyanagi³, Go Iwahana⁴, and Tetsuya Hiyama⁵

¹JAMSTEC

²National Institute for Environmental Studies

³Kumamoto University

⁴International Arctic Research Center, University of Alaska Fairbanks

⁵Nagoya University

November 24, 2022

Abstract

Arctic precipitation (PG) that occurs as rainfall (Pr) or snowfall (Ps) depending on the prevailing climatic conditions results in seasonally specific hydrological events. Climate change can affect the PG- and permafrost-originated water (Pi) regimes, resulting in change to ecohydrological processes. However, the relative influences of source waters (i.e., Pr, Ps, and Pi) on terrestrial hydrological processes have not yet been fully established. Here, we report the development and implementation of a numerical water tracer model designed to quantify changes in the storages and fluxes of the source waters and the hydrogen and oxygen isotopic tracers associated with hydrometeorological events. The presented tracer model was used to illustrate the spatiotemporal variability of the tracers in the surface–subsurface system of a deciduous needleleaf boreal forest, and to separate the contribution rates of the tracer waters to evapotranspiration (ET). Although Ps accounted for 14%–40% of ET and the subcomponents, the contribution rates to soil evaporation and transpiration were significant only during the spring season. The major source water for soil moisture was Pr, which accounted for 80.1% of ET and showed an increasing trend. Additionally, Pr also accounted for 85.7% of transpiration. Under the present conditions of warming permafrost, Pi demonstrated negligibly low impact on ET. The tracer model was shown capable of quantifying the contribution rates of tracer waters to ET, highlighting the advantages of the tracer model for similar quantitative separation regarding future climate change.

1 Tracer model-based quantitative separation of precipitation and permafrost waters used
2 for evapotranspiration in a boreal forest

3

4 Hotaek Park^{1,2,*}, Masahiro Tanoue³, Kimpei Ichiyanagi⁴, Go Iwahana⁵, and Tetsuya
5 Hiyama²

6

7 ¹Institute of Arctic Climate and Environment Research, JAMSTEC, Yokosuka, Japan.

8 ²Institute for Space-Earth Environmental Research, Nagoya University, Nagoya, Japan.

9 ³Center for Global Environmental Research, National Institute for Environmental

10 Studies, Ibaraki, Japan. ⁴Faculty of Advanced Science and Technology, Kumamoto

11 University, Kumamoto, Japan. ⁵International Arctic Research Center, University of

12 Alaska, Fairbanks, USA.

13

14 *Corresponding author: Hotaek Park (park@jamstec.go.jp)

15

16

17 **Key Points**

18

19 ▪ Tracer model separates contributions of precipitation- and permafrost-originated
20 waters to evapotranspiration in deciduous boreal forest

21

22 ▪ Rainfall is a primary source for seasonal and interannual variability of
23 evapotranspiration

24

25 ▪ The isotope process coupled to the tracer model supports the soundness of the
26 partitioned quantification

27

28

29 **Abstract**

30 Arctic precipitation (P_G) that occurs as rainfall (P_r) or snowfall (P_s) depending on the
31 prevailing climatic conditions results in seasonally specific hydrological events. Climate
32 change can affect the P_G - and permafrost-originated water (P_i) regimes, resulting in
33 change to ecohydrological processes. However, the relative influences of source waters
34 (i.e., P_r , P_s , and P_i) on terrestrial hydrological processes have not yet been fully
35 established. Here, we report the development and implementation of a numerical water
36 tracer model designed to quantify changes in the storages and fluxes of the source
37 waters and the hydrogen and oxygen isotopic tracers associated with
38 hydrometeorological events. The presented tracer model was used to illustrate the
39 spatiotemporal variability of the tracers in the surface–subsurface system of a deciduous
40 needleleaf boreal forest, and to separate the contribution rates of the tracer waters to
41 evapotranspiration (ET). Although P_s accounted for 14%–40% of ET and the
42 subcomponents, the contribution rates to soil evaporation and transpiration were
43 significant only during the spring season. The major source water for soil moisture was
44 P_r , which accounted for 80.1% of ET and showed an increasing trend. Additionally, P_r
45 also accounted for 85.7% of transpiration. Under the present conditions of warming
46 permafrost, P_i demonstrated negligibly low impact on ET . The tracer model was shown
47 capable of quantifying the contribution rates of tracer waters to ET , highlighting the
48 advantages of the tracer model for similar quantitative separation regarding future
49 climate change.

50

51 **Plain Language Summary**

52 Although snowfall and rainfall are seasonally different processes, their influence on
53 hydrological processes (i.e., evapotranspiration and river discharge) occurs mainly
54 during the growing season. Quantification of their contributions to hydrological
55 processes is an ongoing scientific problem in Arctic hydrology. Thus, we developed a
56 tracer model, which includes isotopic processes, to separate the contributions of
57 snowfall, rainfall, and permafrost-originated water to evapotranspiration and applied it
58 to a boreal forest. The model simulation suggested that summer rainfall has greatest
59 impact on evapotranspiration, while water from snowfall is strongly implicated in
60 springtime evaporation. Permafrost-originated water is not connected directly to
61 evapotranspiration at this study site. However, the future warming climate could
62 potentially increase the role of permafrost-related water in ecohydrological processes.
63 Thus, the presented water tracer model could potentially provide quantitative
64 assessment of the changes in the physics of water dynamics caused by climate change.
65

66 1. Introduction

67 The effects of recent climate change are more significant in cold regions
68 relative to warm regions. Observational records from Arctic meteorological stations
69 document the evident trend of warming of surface air temperature (T_a) over recent
70 decades (Bekryaev et al., 2010). This warming of T_a has resulted in various changes in
71 cryospheric, hydrological, and ecological processes such as permafrost degradation and
72 deepening of the active layer thickness (ALT) (Park et al., 2016), earlier onset of
73 snowmelt (Kim et al., 2015), and higher vegetation productivity with the development
74 of understory vegetation (Ohta et al., 2014). The enhanced ecohydrological connectivity
75 between soil wetting and canopy greening induced by climate change likely increases
76 water loss to the atmosphere via evapotranspiration (ET). In situ observations (Ohta et
77 al., 2014) and model simulations (Zhang et al., 2010) indicate an increased trend of ET ,
78 which has been particularly significant during the recent two decades when T_a has
79 increased markedly (Bekryaev et al., 2010). Moreover, resultant effects of climate
80 change such as the changed landscape structure and lengthened growing season can
81 alter the ET ratios apportioned to transpiration (E_t), canopy interception (E_i), and
82 evaporation from soil (E_s) and water surfaces. However, the changes to ET and the
83 subcomponents in warming Arctic regions have been poorly understood.

84 Earlier onset of snowmelt and subsequent thawing of frozen soil (Kim et al.,
85 2015) can lead to soil wetting and likely advanced initiation of both E_s and E_t .
86 Moreover, the longer growing season associated with climate change increases the
87 proportion of rainfall in total annual precipitation (P_G) (Bintanja and Andry, 2017),
88 which increases the amount of water input into the soil surface. On entering the soil
89 column, this water mixes with resident older water and/or permafrost-originated water

90 (P_i). The mixing, mobilization, and fluxes associated with this water are likely further
91 enhanced under the situation of a deepening ALT, consequentially altering the fractions
92 of snow water (P_s), rainwater (P_r), and P_i comprising the soil moisture. As the
93 hydrological dynamics of these three source waters are determined by seasonally
94 characteristic events, changes in soil moisture influenced by the source waters can affect
95 water budget components, particularly the processes of E_s and E_t that use soil moisture.
96 Indeed, an isotope observational study identified an isotopic signal indicating plants
97 extract permafrost-originated water under conditions of low soil moisture (Sugimoto et
98 al., 2003). Other studies have presented isotopic evidence showing that plants do not
99 use soil water participating in groundwater recharge and streamflow (Evaristo et al.,
100 2015; Brooks et al., 2010; Goldsmith et al., 2012).

101 Stable water isotopes have been used successfully to understand how water is
102 stored and released in the process of runoff generation, based on the isotopic damping
103 signals from P_G to streamflow (McGuire et al., 2005; Jasechko et al., 2016; Lachniet et
104 al., 2016; Welp et al., 2005). Stable water isotopes have also been used to investigate
105 transpiration–evaporation partitioning, which led to an estimate that transpiration
106 represents 60%–90% of terrestrial ET (Gibson and Edwards, 2002; Good et al., 2015;
107 Jasechko et al., 2013). Good et al. (2015) quantified that 65% of evaporation originates
108 from soils and not surface waters. The capabilities of using isotopes in related research
109 have been amplified further through incorporation of an isotopic module in various land
110 surface models (LSMs) (e.g., Aleinov and Schmidt, 2006; Fischer, 2006; Yoshimura et
111 al., 2006; Sturm et al., 2010; Risi et al., 2016; Hu et al., 2018). Isotope-coupled LSMs
112 have been used to simulate the changes in isotopic composition associated with the
113 storage, flux, and residence time of water flow in the surface–subsurface system.

114 However, the transformations of isotopic compositions might hinder the use of isotope-
115 enabled LSMs for tracking water of individual events. To overcome the limitations of
116 existing LSMs, Hu et al. (2018) developed a new numerical tracer model that tags the
117 water of a P_G event and tracks the pathways of water movement until leaving the system
118 as either ET or runoff. Up to now, however, observations and isotope-enabled tracer
119 models have provided little quantitative information on the fractions of P_r , P_s , and P_i
120 comprising soil moisture or on their contribution rates to hydrological processes,
121 including long-term trends under the effects of climate change.

122 Here, we present a water tracer model to delineate the movements of P_r , P_s ,
123 and P_i in permafrost regions and to quantify their contributions to hydrological
124 processes, including changes in the concentration of hydrogen and oxygen isotopes. In
125 the modeling, the tracer model considers five tracer components as analytical targets
126 and quantifies the changes of the tracer concentrations occurring via the storage and
127 fluxes associated with water movements. The main objective of this study was to
128 quantify the relative contribution rates of P_r , P_s , and P_i source waters to hydrological
129 processes, particularly ET processes, in a boreal larch forest during 1980–2016.
130 Specifically, this study examined the seasonal and interannual variability of the three
131 tracers to explore their responses to hydrometeorological events. Three sensitivity
132 experiments that used different root profile schemes were also conducted to assess the
133 influence of root profiles on E_t , soil moisture, and stable water isotopes.

134

135 **2. Methods**

136 2.1 General model description

137 This study used the coupled hydrological and biogeochemical model
138 (CHANGE; Park et al., 2011, 2018), which is a process-based LSM that comprises a
139 land surface module, biogeochemical dynamics module, and vegetation dynamics
140 module. Thus, the model calculates momentum, heat, water, carbon fluxes, and plant
141 physiology in the atmosphere–vegetation–snow–soil system. CHANGE provides insight
142 into the interactions and feedbacks between ecosystem processes and the ambient
143 atmosphere. The model simulates the accumulation and melt of the snowpack on the
144 land surface, and the meltwater is partitioned consistently into surface runoff and soil
145 infiltration, even during precipitation events. The excess of vertically infiltrated water at
146 either the permafrost table or the bottom soil boundary layer is added to the subsurface
147 runoff. Permafrost is an important component linked to hydrothermal processes in the
148 subarctic terrestrial region. The model resolves soil heat and water flow, and it
149 represents the hydrothermal dynamics of permafrost explicitly through consideration of
150 the freezing/thawing phase transitions in a 1D soil column of 72.4-m depth. Water flow
151 in the permafrost soil layers is represented by parameterization of ice blocking that
152 limits liquid flow. The effects of soil organic carbon (SOC) on the hydraulic and
153 thermal dynamics of the soil are represented through parameterization of the vertical
154 distribution of SOC in the model.

155 The ice content in frozen soil layers reduces the effective porosity and thus
156 decreases soil water availability to plant roots, which consequently increases the
157 probability of water stress. In CHANGE, the soil moisture limitation that represents the
158 stressful conditions associated with drying and/or freezing (i.e., $<-2^{\circ}\text{C}$) is
159 parameterized (value: 0–1). The parameter is coupled to the maximum rate of
160 carboxylation, which varies as a function of leaf temperature, soil moisture, day length,

161 and nitrogen availability (Oleson et al., 2010). Initiation of leaf onset is controlled by a
162 critical degree-day summation of soil temperature at 4 cm depth (White et al., 1997).
163 These parameterizations represent the impact of the thermal states of permafrost on
164 photosynthesis and stomatal conductance, as well as the overall behavior of plant
165 phenology. CHANGE simulates biogeochemical processes across multiple biomes,
166 including the carbon and nitrogen cycling associated with live vegetation, litter, and soil
167 organic matter. The carbon absorbed by photosynthesis is partitioned into leaves, stems,
168 and both fine and coarse roots. Stems and coarse roots also include both live and dead
169 wood components that account for differences in respiration and the carbon:nitrogen
170 ratio. The coupled nitrogen cycle in CHANGE allows consideration of nitrogen
171 limitation on plant productivity, which therefore makes it possible to change the SOC
172 decomposition rate that in turn affects productivity through nitrogen availability. The
173 decomposition rates of SOC are controlled by soil temperature and moisture. These
174 suppressions to the decomposition rate are also dependent on the root distribution.

175

176 2.2 Water tracer model

177 For simulation of water tracers, CHANGE employs an upstream isotopic
178 scheme (Aleinov and Schmidt, 2006), additionally incorporating three water
179 components (i.e., P_r , P_s , and P_i) as tracers. The scheme uses the water fluxes calculated
180 by the LSM, and the advection of the tracers is performed as a sequence of two sweeps
181 (i.e., up and down, indicating the direction of water flow). This allows simplification of
182 the model calculation. As the water flux is directed downward, the tracers move to
183 downstream cells with the water and mix immediately with tracers already in the cell.
184 The tracer amount in that cell is then updated. The tracer amount in a cell is changed

185 only when water is added, and the same amount of tracer is retained until water is
186 removed.

187 In the water cycle, precipitation and dew add water and tracer to the terrestrial
188 system. The canopy layer primarily stores part of the precipitation, while evaporation
189 and drip fall deplete the intercepted water. The latter in turn provides additional water
190 and tracer to the snow or soil surface in the same way as throughfall. Water entering the
191 soil layers sweeps down or up in the direction of water flow. The sweep-down-induced
192 changes in tracer ($C_{i,t}$, kg m^{-2}) and water ($W_{i,t}$, m) at current time step (t) are computed
193 as follows:

$$194 \quad C_{i,t} = C_{i,t-1} - c_{i-1}F_{wi}\Delta t, \quad (1)$$

$$195 \quad W_{i,t} = W_{i,t-1} - F_{wi}\Delta t, \quad (2)$$

196 where c_{i-1} (kg m^{-3}) is the concentration of tracer in the upper layer ($i-1$), F_{wi} is the
197 water flux (m s^{-1}) from the upper layer, and Δt is the time step (s). Soil water content
198 within the i -th soil layer is based on a finite difference approximation of the Richards
199 equation. The moisture content (θ_i) of each layer is updated as:

$$200 \quad \frac{d\theta_i}{dt} = F_{w,i-1} - F_{w,i} - ET_i, \quad (3)$$

201 where $F_{w,i-1}$ and $F_{w,i}$ are the diffusive water flux from the layer above and to the layer
202 below, respectively, and ET_i is the ET extracted from the layer by plant roots and soil
203 evaporation. The vertical water flux (F_w) in the soil layers is computed according to
204 Darcy's law:

$$205 \quad F_w = K_w \frac{\partial}{\partial z}(h + z), \quad (4)$$

206 where K_w is the hydraulic conductivity, z is a vertical coordinate, and h is the matric
 207 potential. The model performs a sweep down for i from 2 to n . In contrast, the sweep up
 208 starts from $i = n - 1$ and ends with $i = 1$:

$$209 \quad C_{i-1,t} = C_{i-1,t-1} + c_i F_{wi} \Delta t, \quad (5)$$

$$210 \quad W_{i-1,t} = W_{i-1,t-1} + F_{wi} \Delta t, \quad (6)$$

$$211 \quad c_i = C_i / W_i. \quad (7)$$

212

213 After completion of both sweeps, the water associated with ET and runoff is
 214 removed from the soil layers and the amount of tracer is updated accordingly. The tracer
 215 concentration (C_{ei}) for evaporation from the canopy, snow, and soil surface is expressed
 216 as follows:

$$217 \quad C_{ei,t} = C_{ei,t-1} + c_i \alpha F_{wi} \Delta t, \quad (8)$$

218 where F_{wi} represents the evaporative flux and α is the kinetic fractionation coefficient
 219 that is the function of wind speed (Merlivat and Jouzel, 1979). Moreover, α is alternated
 220 by an equilibrium fractionation coefficient (Majoube, 1971) because dew condenses on
 221 the surfaces of the canopy, snow, and soil. Additionally, Eq. (8) is equally used to
 222 calculate the changes of tracer concentration in E_t and runoff. The extraction of the
 223 tracers by plant roots in each soil layer is dependent on the LSM-estimated transpiration
 224 amount and the root fraction.

225 The CHANGE model uses a passive characteristic for the stable water isotopes,
 226 that is, there is no fractionation at any phase change in the soil or during transpiration
 227 and runoff. However, we assumed that evaporation of water from the wet canopy, snow,
 228 and soil surface fractionates the isotopes by the kinetic coefficient in Eq. (8),
 229 consequently enriching the isotope rates of the remaining water, whereas evaporative

230 fractionation was excluded from other water tracers by setting $\alpha = 1$. This assumption
231 makes it possible to examine the differences in isotopic ratios in soil moisture, runoff,
232 canopy water, and precipitation.

233 CHANGE calculates the water budget of individual elements (i.e., canopy,
234 snow, and soil) in the LSM, where the water flux between elements is always directed
235 downward. The tracer model that adopts the flow physics is applied separately to the
236 elements. The update of the tracers starts from the canopy and then proceeds in
237 sequence to the snow and the soil, depending on the water fluxes. In the model
238 calculation, P_G is separated into P_r and P_s tracer members that provide the tracer inputs
239 to the elements of the LSM. The tracers move with the water flux and mix completely
240 with the previously stored tracers in individual elements. In the canopy or snow layer,
241 the integrated amount of P_r and P_s is balanced by the stored water amount. In
242 permafrost soil, P_i is added to the tracer member. Water in the permafrost soil
243 experiences the phase change of seasonal freezing and thawing. Thus, P_i occurs during
244 progression of the ALT (i.e., thawing). However, the occurrence of P_i in each soil layer
245 is constrained to happen only once during the calculation period. When the ALT
246 exceeds the maximum ALT identified during the calculation period, including the spin-
247 up run, the ice-melted water at the soil layer is defined as P_i . Once P_i occurs, there is no
248 additional P_i production from the soil layer. Therefore, P_i production is an inherent
249 event in each soil layer. Although P_r and P_s experience seasonal freezing and thawing,
250 the phase changes never affect the change of P_i .

251

252 2.3 Description of study site and observations

253 The observation site, which is underlain with continuous permafrost, is located
254 on the left bank of the middle reaches of the Lena River in eastern Siberia,
255 approximately 20 km north of Yakutsk. The site, which is called “Spasskaya Pad,” is
256 part of an experimental forest of the Institute for Biological Problems of Cryolithozone,
257 Siberian Branch of the Russian Academy of Sciences (SB-RAS). Climatologically
258 (1998–2010), the annual mean air temperature is -10.4°C and the annual mean P_G is
259 259 mm (Ohta et al., 2014). The dominant tree species of the overstory is 160-year-old
260 larch (*Larix cajanderi*) with mean tree height of 18 m, stand density of 840 trees ha^{-1} ,
261 and a leaf area index of 2.0. The forest floor is fully covered by dense cowberry
262 (*Vaccinium vitis-idaea*). The soil at the experimental site is classified as sandy loam. A
263 meteorological observation tower (height: 32 m) was installed at the site, where various
264 meteorological variables were measured at multiple heights. Two eddy-covariance
265 systems were installed at the top of the tower and at the height of 2 m above the forest
266 floor to monitor sensible and latent heat and CO_2 fluxes. Soil moisture and temperature
267 were measured at multiple depths (0–1.2 m) in the soil column. Full descriptions of the
268 site and observations were given by Kotani et al. (2019).

269 Cores of near-surface frozen and unfrozen soil down to 2.4-m depth were
270 sampled at three locations within a larch forest patch in Spasskaya Pad at the end of
271 March 2010. A powered auger (Tanaka TIA-350S) with a 2.5-inch-diameter core
272 sampler was used for the sampling. Sampled cores were truncated to remove
273 contamination, cut into vertical lengths (3–13 cm), and maintained in a frozen state in
274 vacuum-sealed plastic bags until required for laboratory analyses. The isotopic
275 compositions of water (hydrogen and oxygen) were analyzed using the $\text{CO}_2/\text{H}_2/\text{H}_2\text{O}$
276 equilibration method using a Delta V isotope ratio mass spectrometer (Thermo Fisher

277 Scientific, USA, manufactured in Germany) attached to a Gas Bench (Thermo Fisher
278 Scientific, USA) at Hokkaido University, Japan (Ueta et al., 2013). These data were
279 expressed as $\delta^2\text{H}$ or $\delta^{18}\text{O}$ values, defined as $\delta_{\text{Sample}} (\text{‰}) = (R_{\text{Sample}}/R_{\text{VSMOW}} - 1) \times 1000$,
280 where R is the isotope ratio of water ($^2\text{H}/^1\text{H}$ or $^{18}\text{O}/^{16}\text{O}$), and subscripts “Sample” and
281 “VSMOW” refer to the samples and standard (i.e., Vienna Standard Mean Ocean
282 Water), respectively. The analytical errors for the entire procedure were within 2‰ and
283 0.2‰ for $\delta^2\text{H}$ and $\delta^{18}\text{O}$, respectively. The analyzed isotope ratios of all samples within
284 each 30-cm depth were integrally averaged for comparison with the simulated values.

285

286 2.4 Model application

287 To create the daily model forcing data for the period 1980–2016, observations
288 at the study site were combined with ERA-Interim reanalysis data from the European
289 Centre for Medium-Range Weather Forecasts. These data include the bias-corrected
290 monthly Climate Research Unit temperature dataset and the Global Precipitation
291 Climatology Project precipitation dataset, which were used as the baseline to construct
292 the meteorological forcing data for running the model. Miyazaki et al. (2015) describe
293 the generation of the forcing data in detail.

294 CHANGE needs isotopic forcing data of P_G and atmospheric water vapor.
295 However, continuous, long-term observational records of such isotope data are lacking.
296 There is currently no alternative to a numerical model for preparing the isotopic forcing
297 data for running the model. The Scripps Isotopes-incorporated Global Spectral Model
298 (IsoGSM) has been used to produce a long-term global dataset of stable water isotopes
299 (Yoshimura et al., 2008). Thus, the results from the grid nearest to the experimental site
300 were selected and used as forcing data for CHANGE. However, the daily P_G events

301 between our forcing data and IsoGSM were found inconsistent, which would have
302 likely resulted in uncertainties regarding the model simulation. Therefore, weighted
303 monthly averages of the IsoGSM-simulated isotopic values of P_G and specific humidity
304 were calculated, and the averaged values were applied homogeneously to the daily P_G
305 and specific humidity. The monthly averaged isotopic values of the IsoGSM-simulated
306 P_G were compared with records of observations taken at Yakutsk station over a 5-year
307 period (1996–2000), archived as part of the Global Network of Isotopes in Precipitation
308 by the International Atomic Energy Agency. The comparison revealed general
309 overestimation by the IsoGSM for the two isotopic components (Fig. 1), which would
310 likely cause uncertainty in the simulated isotopic processes. Therefore, the IsoGSM-
311 simulated isotopic values used for the CHANGE simulations were adjusted to the
312 observations using a scaling coefficient of 1.3.

313 A static land cover type of boreal deciduous needleleaf forest was defined for
314 the simulation, while the vegetation phenology was prognostic based on estimated
315 carbon and nitrogen fluxes. Measured fractions of sand, silt, and clay were set initially
316 to those of the vertical soil texture profile, and the SOC profile was simulated at each
317 time step. On the basis of these soil properties, the model estimated the thermal and
318 hydraulic properties of the soil. Through the spin-up run, the model determined a
319 dynamic equilibrium of total ecosystem carbon and nitrogen contents with the
320 prescribed climate, repeating for 1200 years using the detrended forcing data of the
321 initial 20 years and a CO₂ concentration of 350 ppm. After completing the spin-up, the
322 atmospheric CO₂ concentration in the simulations was set to vary over time based on
323 global observational records. The minimum oxygen (–25‰) and hydrogen (–190‰)
324 isotopic values obtained from the analyzed soil cores were set as the initial isotope

325 values of all the soil layers. The stable water isotopes of the soil layers were updated
326 through mixing with the P_G inputs and evaporation fractionation during the spin-up
327 period. Ultimately, the influence of the initialization on the simulated results was minor,
328 at least in the active layers.

329 Plant roots extract soil moisture, resulting in a vertically heterogeneous water
330 profile. The root profile readily affects soil moisture as well as tracer amounts. To
331 explore how different root profiles might affect E_t and the tracers, three numerical
332 experiments were designed. In the control simulation (S_{CN}), the cumulative root
333 distribution was given by $(1 - \beta^z)$, where z is the soil layer thickness and β is a
334 vegetation-dependent coefficient (Jackson et al., 1996), which is assumed time
335 invariant. As β does not change with vegetation age and/or root biomass, the rooting
336 depth remains constant irrespective of plant size. The second simulation (S_{MT}) used the
337 root algorithm adopted from Williams et al. (2001). In this algorithm, plant root
338 distribution is determined by three factors: the time-variant total fine root biomass,
339 maximum root biomass per unit volume that is assumed to occur at the soil surface, and
340 depth of rooting. The root biomass per unit volume decays exponentially in terms of
341 root length with depth. The third simulation (S_{AB}) was based on the model of Arora and
342 Boer (2003), which proposed a methodology for parameterizing root distribution as a
343 function of root biomass. The S_{AB} model is intended to overcome some of the
344 limitations in the prescription of a static root distribution profile in dynamic vegetation
345 models. In the representation, root distribution and rooting depth both evolve and
346 increase as the root biomass increases, as would be expected intuitively. The soil
347 column (70.4 m) in CHANGE is discretized into 31 layers. The soil surface (e.g., ~0.37
348 m) over which the soil water gradient is generally strong forms six soil layers based on

349 an exponential equation (Oleson et al., 2010), and then the soil layers have a 0.2-m node
350 depth to 3.2 m. The deepest remnant layers in turn form thicker node depths based on
351 the exponential equation.

352

353 **3. Results**

354 3.1 Model performance

355 The CHANGE-simulated results for energy, water, and carbon fluxes, *ET*, and
356 soil moisture and temperature profiles, which have previously been validated against
357 observational records, showed statistically satisfactory performance for seasonal and
358 interannual variability in different climatic zones, including the Spasskaya Pad study
359 site (Park et al., 2011, 2018). Here, the validation of model performance using
360 observations was confined to the simulated isotopic results because the isotope process
361 was newly coupled to the model. The model-simulated soil-isotope profiles were
362 averaged for March 2010 when the soil cores were sampled. The monthly averaged
363 simulations were compared with the median values of the analyzed soil cores (Fig. 2).
364 The three simulations that have vertically different root distributions (Fig. 2c) show
365 similar profiles from the surface to the depth of 2.4 m (Fig. 2a, b). The comparison
366 indicates that the simulated isotope ratios (i.e., $\delta^{18}\text{O}$ and $\delta^2\text{H}$) distribute within or close
367 to the interquartile range (IQR) of the observations from the surface to 1.2 m (Fig. 2a,
368 b), where the observed and simulated isotope ratios are depleted with depth. However,
369 at depths of 1.2–1.8 m, where soil moisture is generally saturated owing to permafrost
370 table blocking of water infiltration, the model simulated enriched isotopes in
371 comparison with the observations of depletion with depth. CHANGE tends to estimate

372 higher hydraulic conductivity and porosity owing to the SOC and vertically consistent
373 soil texture composition. The higher hydraulic conductivity likely enhances the mixing
374 of summer P_G -originated heavy isotopes in the ALT.

375 A previous study provided oxygen isotopic ratios of soil water in three soil
376 layers and of sap water in plants sampled during the growing season during 1998–2000
377 at the same study site (Sugimoto et al., 2003). We used the analyzed isotope ratios of
378 two soil layers (0–0.3 and 0.3–0.6 m) and sap water for further validation of the
379 simulations. The modeled isotope ratios were averaged for 10 days prior to the
380 observation date. Although comparison of the surface soil water (Fig. 2d) shows
381 agreement between the simulations and observations, larger deviations are specifically
382 identified at the three simulated events (e.g., August and September 1999 and May
383 2000). The deviations are partially attributable to the influence of biased monthly
384 precipitation isotopic forcing; for example, the model was forced by precipitation of
385 -19.9‰ in August 1999, which was lighter than observed, that is, -15.7‰ (Sugimoto
386 et al., 2003). The P_G isotopic ratios for the CHANGE simulations were corrected for
387 bias using the observed values; however, some deviations remained. The deviations in
388 the surface soil layer that had the largest fraction of roots (Fig. 2c) were consequently
389 associated with errors (-2.2‰ , root mean square error) in transpiration (Fig. 2f).

390

391 3.2 Impacts of separated source waters on evapotranspiration

392 The simulated daily vertical soil moisture and separated source waters were
393 averaged for the entire study period, and the averaged seasonal variability is presented
394 in Fig. 3. In spring, the frozen soil thaws and saturates the soil surface (Fig. 3a) with the

395 inflowed P_s (Fig. 3b). The derived P_s , which is mainly stored in the surface soil layers,
396 that is, to approximately 10-cm depth during April–June (Fig. 3b), is also pushed down
397 by incoming summer P_r during the same period and contributes to the higher level of
398 soil moisture at the depth of 0.8 m or deeper (Fig. 3a). The P_r from the previous autumn
399 that exists in the upper layers is displaced by the incoming P_s and flows downward,
400 partially infiltrating to depths of 2.0 m (Fig. 3c). The surface soil moisture is sourced
401 primarily from summer P_r of the current year, whereas the deeper soil contains waters
402 of varying ages. In autumn, the fraction of P_r in the surface soil moisture increases
403 owing to low evaporation and transpiration, and this higher level of soil moisture is
404 maintained until the following spring. Overall, P_i is primarily distributed at the depth of
405 1.7–2.1 m (Fig. 3d), reflecting the signal of the ALT progression during the simulation
406 period.

407 Snow meltwater is distributed mainly from the surface to 10-cm depth during
408 spring, accounting for 40% or more of the gross soil moisture, whereas the fraction in
409 deeper layers is considerably lower. Overall, the main source of soil moisture within the
410 ALT is P_r , which accounts for 80% or more over the entire period, except in the surface
411 layers in spring. The maximal fraction of 95% occurs in the surface layers owing to
412 autumnal rainfall. Overall, P_i at depths of 1.7–2.1 m accounts for approximately 10% of
413 the soil moisture.

414 The averaged seasonal variations of ET and the subcomponents with the
415 contribution amounts of the separated source waters are displayed in Fig. 4. It can be
416 seen that ET shows typical seasonality with a summer peak, consistent with E_t that
417 accounts for 63.3% of ET (Table 1). Temporally, E_t increases rapidly with leaf opening
418 and the increase of T_a , reaching the maximum value in July, which is different to the

419 gradual increase of E_i . Approximately 60% of E_i is apportioned by rainfall (Table 1).
420 Meanwhile, E_s increases from early spring (when the frozen soil begins to thaw),
421 reaches the maximum value in May, and thereafter decreases markedly owing to the
422 reduction in solar radiation induced by the increasing leaf amount. The maximal value
423 of E_s in spring is a general phenomenon in cold regions (Park et al., 2008).

424 The source waters that contribute to E_s show interesting seasonal variations. In
425 spring, E_s simultaneously evaporates P_r and P_s from the soil surface (Fig. 4c). When P_s
426 covers the soil surface, evaporation of P_r is temporally restrained. During April–May,
427 P_s accounts for 47% of E_s . Once the P_s in the soil surface is largely evaporated,
428 evaporation of P_r restarts and accounts for most of E_s during summer. In summer, the P_s
429 that enters the surface soil layers (Fig. 3b) is transpired by plants; however, the
430 contribution of P_s to E_t is not larger than that of P_r , which accounts for 85.7% of E_t
431 (Table 1). The largest uptake of P_r by plants occurs in the soil layers in which the roots
432 are fractionally maximal (Fig. 5). The three experiments show evident differences in the
433 vertical distribution of E_t . The maximal E_t values in individual experiments are present
434 at the same soil layers that the root fraction is maximal (Fig. 2c). For example, S_{CN}
435 presents the maximal value of E_t at 10-cm depth, whereas it is at 40-cm depth in S_{MT} .
436 Uptake of water by plant roots is strongest in June and July (Fig. 5) when plant
437 productivity is most vigorous (Park et al., 2011). However, the difference in the annual
438 E_t between the three experiments that show vertically different root profiles is not large
439 (Table 1). Overall, P_r accounts for 80.1% of ET (Table 1). The contribution of P_i to ET
440 is negligible because P_i is stored mainly in the deepest soil layers (Fig. 3d) where roots
441 are nonexistent (Fig. 2c).

442

443 3.3 Isotope variability

444 The simulated isotopes in the soil column were averaged over the study period,
445 and their seasonal and vertical variations are displayed in Fig. 6. Both $\delta^{18}\text{O}$ and $\delta^2\text{H}$
446 show similar seasonal variation in their vertical profiles and evident delineation of the
447 signal of the translatory flow of water movement; in other words, P_G -originated water
448 entering the soil displaces the water that is already present, pushing it deeper into the
449 soil (Hewlett and Hibbert, 1967; Horton and Hawkins, 1965). In spring, the inflowing
450 P_s displaces the water resident in the surface layers and depletes the isotope ratios.
451 Then, the downward movement of the surface water enriches the isotopes of the soil
452 below. Meanwhile, the P_r -induced translatory flow in summer isotopically depletes the
453 deeper soil via the inflow of P_s from the surface layers. In turn, the autumn P_r depletes
454 the isotopes of the surface soil, and the resultant isotope ratios in autumn remain until
455 the following spring. The d-excess also displays similar seasonal variability to that
456 identified in relation to $\delta^{18}\text{O}$ and $\delta^2\text{H}$. Isotopically enriched summer P_G results in the
457 lowest d-excess in the upper soil layers, and the kinetic fractionation with evaporation
458 also contributes to the lowest d-excess in the surface layer (Fig. 6c).

459 Winter P_G results in the lowest value of $\delta^{18}\text{O}$ for the snowpack (min.: -33‰)
460 (Fig. 7a). The surface soil water is displaced by the melted P_s , resulting in a depleted
461 $\delta^{18}\text{O}$ value in late April (Fig. 7a), which is eventually linked to the depleted E_s $\delta^{18}\text{O}$
462 (Fig. 7b) owing to the largest loss of P_s by E_s (Fig. 4c). Then, E_s $\delta^{18}\text{O}$ is enriched during
463 summer under the influence of heavy P_r $\delta^{18}\text{O}$ before returning to a more depleted level
464 in autumn (Fig. 7a). Meanwhile, E_t $\delta^{18}\text{O}$ generally evolves toward summer (Fig. 7b)
465 because E_t preferentially uses the isotopically light and stable moisture of deeper soil
466 layers (Fig. 5) owing to the relatively large fraction of roots (Fig. 2c). The influence of

467 P_s on the isotopes of E_t is not large, causing instead slightly depleted $\delta^{18}\text{O}$ in May (Fig.
468 7b). The median of the monthly averaged E_t $\delta^{18}\text{O}$ (-19.5‰) is similar to that of soil
469 water in the surface layers (-19.3‰), with similar variability expressed by an IQR of
470 1.1% and 1.9%, respectively (Fig. 8), indicating stronger hydrological connectivity
471 between them. Meanwhile, the simulated homogeneous isotope ratios in soil water at
472 depths of 0.3–1.4 m (Figs. 2 and 6) likely result in a relatively small IQR for E_t $\delta^{18}\text{O}$.
473 The distributions of E_t $\delta^{18}\text{O}$ in the boxplots (Fig. 8) indicate a range of -21.1‰
474 (minimum) to -17.2‰ (maximum), which is generally consistent with the range
475 -22.5‰ to -16.0‰ observed in sap water during 1998–2000 at the same site (Sugimoto
476 et al., 2003).

477 Canopy-intercepted water shows the largest IQR (i.e., 13.4%) for $\delta^{18}\text{O}$ (Fig. 8),
478 representing the variability caused by both the isotopic depletion by condensation in the
479 cold season and the enrichment of heavy isotopes by evaporation fractionation in
480 summer. Snowpack shows more depleted isotopes and thus a lower median value
481 (-31.1‰ for $\delta^{18}\text{O}$) than P_G (-28.7‰), and it plots outside the median values of other
482 processes (i.e., E_s , E_t , and soil water). However, the minimum value of snowpack in the
483 boxplot is larger than that of P_G and canopy water (Fig. 8), indicating isotope
484 enrichment by sublimation fractionation from the snow surface and the addition of
485 isotopically enriched snow falling from the canopy. The signal of evident enrichment of
486 the median $\delta^{18}\text{O}$ from P_G to soil water confirms the effects of evaporation and water
487 mixing in the hydrological processes on the isotope changes (Ala-aho et al., 2018).

488 Signals of evaporation in hydrological processes can be explored using d-
489 excess values. The d-excess median for water storages (i.e., canopy, snow, and soil)
490 tends sequentially to reduce along the water flow from P_G to the soil system, plotting

491 below the median of P_G d-excess, and the d-excess values in ET (E_i , E_s , and E_t), closely
492 associated with summer P_G , are also lower (Fig. 8). Overall, E_s has the lowest d-excess
493 values (median: -1.5‰), indicating a strong evaporation signal. The snowpack d-
494 excess, averaged over the cold season from autumn to spring (8.7‰), is lower than the
495 median value of 11.8‰ observed in the coldest February/March in Siberian regions
496 (Kurita et al., 2005; Vasil'chuk et al., 2016; Ala-aho et al., 2018), despite the lower
497 isotopic ratios (i.e., -31.1‰ for $\delta^{18}\text{O}$) than observed (i.e., -28.8‰ for $\delta^{18}\text{O}$) (Vasil'chuk
498 et al., 2016). The volume-weighted average of P_G d-excess is 12.4‰ (Fig. 8), which is
499 higher than the value (2.9‰) of the Global Network of Isotopes in Precipitation samples
500 from Yakutsk. The local meteoric water line—the regression line of all processes in
501 Fig. 8—has slope of 7.90 , similar to that (7.81) of precipitation samples from Yakutsk
502 obtained from the Global Network of Isotopes in Precipitation.

503

504 3.4 Interannual variability of evapotranspiration

505 In cold regions, T_a is a major driving factor for ET . The simulated ET shows an
506 increasing trend (0.18 mm yr^{-1} , $p < 0.10$) during 1980–2016 (Fig. 9), which is a
507 response to the increasing T_a (Fedorov et al., 2014). Overall, ET averaged for the three
508 experiments during the study period was 187 mm yr^{-1} (Table 1), which explained 95%
509 of the observed annual mean ET (196 mm) for 1998–2006 (Park et al., 2011). The
510 subcomponents of ET increase consistently, although they are statistically insignificant.
511 The increase of T_a causes greater plant productivity and a larger leaf area index (Park et
512 al., 2011) associated with the higher E_t and water storage on leaf surfaces, leading to
513 higher E_i . Meanwhile, the larger leaf area decreases solar radiation at the forest floor,

514 consequently reducing E_s with an insignificantly negative trend of $-0.005 \text{ mm yr}^{-1}$.
515 Observations have identified earlier thawing of frozen soil (Kim et al., 2015; Fedorov et
516 al., 2014) correlating to larger E_s . Therefore, the climate-warming-induced decrease of
517 solar radiation and earlier onset of soil thawing have a competitive relationship
518 regarding E_s . The contribution of P_r to ET increased significantly during the study
519 period (0.23 mm yr^{-1} , $p < 0.01$), whereas that of P_s decreased slightly ($-0.005 \text{ mm yr}^{-1}$,
520 statistically insignificant).

521

522 3.5 Sensitivity analysis

523 The three experiments characterized by vertically different root profiles
524 resulted in small difference in the annual E_t ; S_{MT} with the deepest root depth (Fig. 2c)
525 transpired 3 mm more soil water than either S_{CN} or S_{AB} (Table 1). To investigate the
526 influence of root depth on E_t , two sensitivity experiments with root depth extending to
527 1.56 m were conducted based on the parameters and conditions of S_{CN} . Specifically, the
528 first experiment excluded the soil freezing stress by permafrost for plant roots
529 connected to photosynthesis and stomatal conductance (S_{TE}), whereas the second
530 experiment did consider the stress (S_{TI}). The sensitivity experiments produced E_t values
531 of 117.5 mm for S_{TE} and 117.2 mm for S_{TI} , showing similar values to S_{CN} (Table 1)
532 despite the large differences in root depth. The CHANGE-simulated ALT was in the
533 range of 1.5–1.8 m in all experiments, in which the soil moisture within the ALT was
534 generally high (Fig. 3a). These conditions make plant roots free from the stresses of
535 both permafrost-related freezing and low soil moisture. Although the root length was
536 extended, the root fraction in the deepest soil layers was very low. Therefore, the impact

537 of extended roots on E_t was not large. In temperate or tropical regions where soil
538 drought is frequent, root extension to deeper soil depths is efficient for E_t absorbing
539 water from the deepest soil layers (Yang et al., 2016).

540 CHANGE also simulated isotope profiles in the three experiments that were
541 similar to the observations in March 2010 (Fig. 2a, b). However, a difference between
542 the simulations was found in the surface soil layers of 0–30 cm, in which S_{CN} with the
543 largest root fraction produced slightly enriched isotopic values relative to S_{MT} and S_{AB} ,
544 suggesting possible impact of the root structure on isotope variability. Thus, the isotopic
545 value of S_{CN} was in turn compared with that of S_{TE} and S_{TI} . In comparison with S_{CN} , the
546 anomalous $\delta^{18}O$ profiles in S_{TE} and S_{TI} show enriched isotopic values in all soil layers
547 except the surface layer (Fig. 10). The deepened roots of S_{TE} and S_{TI} absorbed further
548 water despite having a lower root fraction in the deeper layers, driving more downward
549 mobility of isotopically heavy water from the upper soil layers. The resultant inflow of
550 summer precipitation-originated warm water to the lower soil layers increased the ALT;
551 consequently, the ALT of S_{TE} and S_{TI} was 10 cm deeper than that of S_{CN} . The water
552 movement during ALT development caused an increase in heavy isotope ratios in the
553 deepest soil layers (Fig. 10). These results indicate a hydrological function of the root
554 structure associated with the fluxes of soil water.

555

556 **4. Discussion**

557 Previous large-scale hydrological work focused on high-latitude landscapes has
558 successfully isolated the volumetric contributions of snowmelt, groundwater, and
559 summer rainfall to streamflow, and established relationships between seasonal water

560 balance components and climatic variables (Serreze et al., 2002; Ye et al., 2004; Yang
561 et al., 2004; Tan et al., 2011). The results revealed representatively that P_s is the
562 dominant runoff generation process, accounting for approximately 60% in the Kolyma
563 watershed of northeastern Siberia that is underlain by continuous permafrost (Welp et
564 al., 2005) and in the Yukon (Canada) and Alaska (USA) (Lachniet et al., 2016). Unlike
565 its identified impact on runoff, the influence of P_s on ET has yet to be fully assessed.
566 Here, we provide quantitative evidence that P_s accounts for 14%–40% of ET and the
567 subcomponents (Table 1) in eastern Siberia, that is, considerably lower in comparison
568 with runoff. When snow melts, the underlying soil remains frozen and the ALT is low.
569 While frozen soil promotes rapid routing of P_s in a landscape generating infiltration-
570 excess surface runoff (Woo et al., 2008), part of P_s wets the surface soil (Fig. 3) and
571 thus contributes to ET . The distribution of $\delta^{18}\text{O}$ presents lower probability for utilization
572 of a snow-derived isotopically lighter water by E_s and E_t than reliance on heavier water
573 derived from summer rainfall (Fig. 11).

574 As ET occurs primarily during the warming season, the influence of summer
575 rainfall on ET is intuitively large. At the study site, rainfall that accounted for 65% of
576 annual P_G showed a trend of increase (0.61 mm yr^{-1} , $p < 0.1$) during the study period.
577 Increased rainfall primarily reduces the limitations of moisture availability for ET . In
578 addition, a warming climate induces a longer growing season (Kim et al., 2015; Park et
579 al., 2016) that is beneficial for enhanced ET . Summer rainfall tends to be stored in
580 surface soil layers (Fig. 3) with high porosity owing to the effects of SOC, and the water
581 is extracted immediately by the higher fraction of roots (Fig. 2c). In turn, rainfall events
582 supply water to the dried surface layers, and this water is generally of relatively young
583 age with isotope ratios similar to those of P_G (Fig. 6), identified by the higher use of an

584 isotopically heavier source water by E_s in the summer (Fig. 11) and thus lower d-excess
585 (Fig. 8). Owing to the larger water consumption in the surface soil layers, summer
586 rainfall has comparatively low opportunity to exchange with water of the deeper soil.
587 Thus, we did not find signals of significant isotopic enrichment as evidence of the
588 largest movement of summer rainfall into the deeper soil in the control simulation (Fig.
589 6). The smaller isotope changes of soil moisture resulted in a tight distribution of E_t
590 $\delta^{18}\text{O}$ of between -22‰ and -16‰ (Fig. 11) with the steady state flux during the
591 growing season (Fig. 7b). However, the extension of root depth caused isotopic
592 enrichment at the deeper soil layers because root water uptake induces water inflow
593 from the upper layers (Fig. 10). This is likely amplified by larger root biomass and ALT
594 under a warming climate, including further implication of P_i to soil water flux and E_t .

595 Previous studies have examined the impact of autumn P_G on permafrost
596 warming via snow insulation (Park et al., 2015), as well as its connectivity to spring
597 streamflow via lake and wetland water storage (Hayashi et al., 2004). However,
598 understanding the physics of how autumn rainfall that is generally stored in the surface
599 layers as frozen water (Fig. 3c) is related to ET in the following summer and its
600 quantitative assessment is lacking. Here, our tracer model illustrated a physical
601 mechanism via which autumn rainfall is connected to the ecohydrological processes of
602 the following summer. In autumn, the soil generally becomes frozen before the
603 autumnal rainfall infiltrates into the deeper soil. Therefore, autumn rainfall spends the
604 winter as ice in the upper soil layers. Part of the autumn rainfall is used directly by E_s
605 during snow melting (Fig. 4). The entering P_s pushes the autumn rainfall in the surface
606 soil layers downward (Fig. 6). The downward movement of autumn rainfall contributes
607 to spring soil wetness (Fig. 3a) and then to higher summer ET . Strictly, the flux of

608 spring P_s enhances the mixing of autumn rainfall with the existent soil water in the
609 deeper layers and then connects to the summer ET . Unfortunately, the tracer model
610 remains deficient in illustrating the entire pathway via which water of each P_G event
611 leaves the surface–subsurface system as streamflow or ET . Therefore, the tracer model
612 cannot provide information on the quantitative contribution of seasonal P_G to ET , which
613 will be addressed in future research.

614 The progress of the ALT reflects the melting of ground ice in the permafrost
615 table. In this study, P_i comprised approximately 10% of the soil moisture in the lower
616 ALT boundary layer (Fig. 3). As P_i is located below the root depth, access to P_i by
617 plants is considerably restricted. Consequently, we found nearly no contribution to E_t by
618 P_i . Under dry conditions, plants extract water from deeper soil layers to reduce moisture
619 stress (Nepstad et al., 1994; Yang et al., 2016). The study site has a dry climate owing
620 to the reasonably low P_G . However, soil moisture within the ALT generally maintains
621 wet conditions beyond the wilting point (Fig. 3a). Thus, this soil moisture likely reduces
622 the dependence of ET upon the P_i of the deeper soil. The deeper soil layers in which P_i
623 is stored usually record soil temperatures close to 0°C. The cold temperature likely
624 limits the activity of water extraction by roots. Indeed, the S_{MT} experiment with the
625 deepest root depth of 1.0 m resulted in annual E_t that was 3 mm greater than in S_{AB} with
626 the shallowest root depth (Table 1), suggesting relatively low impact of the different
627 root profiles on annual E_t between the wet and cold permafrost regions. However,
628 LSMs have projected dry soil moisture in the Arctic regions under the conditions of
629 future climate change (Andresen et al., 2020); therefore, we expect that the contribution
630 of P_i to E_t will probably increase further.

631 The tracer model is a powerful tool with which to represent more
632 comprehensively the physical dynamics of P_G -originated waters and the isotopes in the
633 surface–subsurface system. The simulated isotope variations present a seasonal shift in
634 the reliance of ET on an isotopically lighter water supply in spring, followed by a
635 transition toward the use of an isotopically heavier source water in summer (Fig. 7). In
636 particular, the soil surface layers in early spring have experienced strong mixing of P_s
637 and P_r , showing their competitive contributions to E_s during the shortest period (Fig.
638 4c). CHANGE simulated the deficient isotope values in the phase of P_s priority for E_s
639 and soil water and then their enrichment governed by P_r (Fig. 7). This simulation
640 alternatively supports a reasonable estimation of the partition of P_G -originated ET
641 source waters (Fig. 4), seldom validated by observational data. For the model
642 calculation, isotopic forcing data are required to drive the tracer module. However, few
643 in situ long-term observational data are currently available. Alternatively, we used
644 monthly isotopic ratios produced by an isotope climate model as the forcing. The use of
645 monthly isotopic data was probably inappropriate for realistic representation of the
646 concentration changes of the isotope compositions in each P_G event. Nevertheless, as
647 the main work of this study does not complete the transpiration–evaporation
648 partitioning based on the simulated isotope ratios, uncertainties related to the monthly
649 forcing data might not preclude meaningful analysis on the separation of the source
650 waters used for ET . Furthermore, the model did appropriately simulate the isotopic
651 composition changes through mixing, advection, diffusion, and related fractionation in
652 water transport in the surface–subsurface continuum.

653 Previous studies have identified dual water flows in the soil system, that is,
654 water moves slowly through soil micropores and rapidly through preferential pathways

655 that bypass the soil matrix (McDonnel, 1990; Buttle and McDonald, 2002; Hrachowitz
656 et al., 2013, 2016). Unlike previous findings, our tracer model assumed that tracer
657 transport was proportional to the water flux and that complete mixing occurred in each
658 soil layer. Homogeneous mixing likely results in earlier arrival of tracers to a certain
659 depth with a more dispersed transit time distribution than observed (Hu et al., 2018).
660 Consequently, the model assumptions could increase the influence of incoming tracer
661 flux on changes in tracer concentrations. For example, the simulated isotope ratios
662 showed large deviations against observations at 1.2–1.8-m depth (Fig. 2a, b). The
663 deviation is probably an example associated with the model assumptions, combined
664 with the influence of the monthly isotopic forcing data. To represent physically the
665 heterogeneous water flow, Hu et al. (2018) introduced a parameterization of a
666 dynamical partial mixing by separating the total storage in each soil layer into
667 active/mobile and passive/immobile compartments, and the model appropriately
668 implemented the ecohydrological separation of soil water found by isotopic studies
669 (Brooks et al., 2010; Evaristo et al., 2015). The parameterization suggested by Hu et al.
670 (2018) represents a reasonable benchmark with which to assess improvement of the
671 deficiency of our tracer model.

672

673 **5. Conclusions**

674 We developed a water tracer model specifically designed to estimate the
675 storage and fluxes of P_G - and permafrost-originated waters of individual
676 hydrometeorological events based on changes in isotopic concentration via water
677 transport. In comparison with existing LSMs that incorporate isotopes, our tracer model

678 explicitly separates the contributions of the partitioned tracers to water balance
679 components. The model implementation considers that P_r is the major contributor to ET
680 in a deciduous needleleaf boreal forest, while the contribution of P_s is acknowledged as
681 restrictively significant to E_s and E_t in early summer because of the blocking effect of
682 permafrost on water infiltration. The simulated isotope ratios contribute to reduction of
683 uncertainties regarding the separate contributions of P_G -originated source water to ET ,
684 which have yet to be validated with observed data. Future climate warming will induce
685 earlier and deeper soil thawing that will likely increase the quantity of P_s entering the
686 soil and hence result in a larger contribution to ET . By contrast, the warming climate
687 will increase the fraction of summer rainfall in P_G (Bintanja and Andry, 2017), which
688 will also contribute to larger ET . We therefore expect that P_r will remain the largest
689 influence on ET in the future. The future climate could potentially increase the roles of
690 permafrost-related water in ecohydrological processes, but our understanding of which
691 remains considerably lacking. The presented water tracer model is certainly a useful
692 tool with which to distinguish quantitatively the changes of the water dynamic physics
693 caused by climate change.

694

695 **Acknowledgments**

696 This study was partly supported by the Japan Society for the Promotion of Science
697 KAKENHI Grant Number 17H01870 and 19H05668. It was also supported by JST
698 Belmont Forum Grant Number JPMJBF2003, Japan. We thank James Buxton MSc
699 from Edanz Group (<https://en-author-services.edanz.com/ac>) for editing a draft of this
700 manuscript. Data analyzed in this study will be opened through the data archive system
701 of JAMSTEC.

702

703 **References**

704 Ala-aho, P., C. Soulsby, O. S. Pokrovsky, S. N. Kirpotin, J. Karlsson, S. Serikova, S. N.
705 Vorobyev, R. M. Manasypov, S. Loiko, and D. Tetzlaff, 2018: Using stable isotopes to
706 assess surface water source dynamics and hydrological connectivity in a high-latitude
707 wetland and permafrost influenced landscape. *J. Hydrol.*, **556**, 279–293,
708 <https://doi.org/10.1016/j.jhydrol.2017.11.024>.

709 Aleinov, I., and G. A. Schmidt, 2006: Water isotopes in the GISS ModelE land surface
710 scheme. *Global Planet. Change*, **51**, 108–120.

711 Andresen, C. G., D. M. Lawrence, C. J. Wilson, A. D. McGuire, C. Koven, K. Schaefer,
712 E. Jafarov, S. Peng, X. Chen, I. Gouttevin, E. Burke, S. Chadburn, D. Ji, G. Chen, D.
713 Hayes, and W. Zhang, 2020: Soil moisture and hydrology projections of the permafrost
714 region – a model intercomparison. *Cryosphere*, **14**, 445–459, [https://doi.org/10.5194/tc-](https://doi.org/10.5194/tc-14-445-2020)
715 [14-445-2020](https://doi.org/10.5194/tc-14-445-2020).

716 Aora, V. K., and G. J. Boer, 2003: A Representation of Variable Root Distribution in
717 Dynamic Vegetation Models. *Earth Interact.*, **7**, 1–19, [https://doi.org/10.1175/1087-](https://doi.org/10.1175/1087-3562(2003)007<0001:AROVRD>2.0.CO;2)
718 [3562\(2003\)007<0001:AROVRD>2.0.CO;2](https://doi.org/10.1175/1087-3562(2003)007<0001:AROVRD>2.0.CO;2).

719 Bekryaev, R. V., I. V. Polyakov, and V. A. Alexeev, 2010: Role of polar amplification
720 in long-term surface air temperature variations and modern Arctic warming. *J. Clim.*,
721 **23**, 3888–3906.

722 Bintanja, R., and O. Andry, 2017: Towards a rain-dominated Arctic. *Nature Clim.*
723 *Change*, **7**, 263–267, <https://doi.org/10.1038/nclimate3240>.

724 Brooks, J. R., H. R. Barnard, R. Coulombe, and J. J. McDonnell, 2010: Ecohydrologic
725 separation of water between trees and streams in a Mediterranean climate. *Nature*
726 *Geosci.*, **3**, 100–104, <https://doi.org/10.1038/ngeo722>.

727 Buttle, J. M., and D. J. McDonald, 2002: Coupled vertical and lateral preferential flow
728 on a forested slope. *Water Resour. Res.*, **38**, 1060,
729 <https://doi.org/10.1029/2001WR000773>.

730 Evaristo, J., S. Jasechko, and J. J. McDonnell, 2015: Global separation of plant
731 transpiration from groundwater and streamflow. *Nature*, **525**, 91–94,
732 <https://doi.org/10.1038/nature14983>.

733 Fedorov, A. N., R. N. Ivanova, H. Park, T. Hiyama, and Y. Iijima, 2014: Recent air
734 temperature changes in the permafrost landscapes of northeastern Eurasia. *Polar Sci.*, **8**,
735 114–128, <https://doi.org/10.1016/j.polar.2014.02.001>.

736 Fischer, M. J., 2006: iCHASM, a flexible land-surface model that incorporates stable
737 water isotopes. *Global Planet. Change*, **51**, 121–130.

738 Gibson, J. J., and T. W. D. Edwards, 2002: Regional water balance trends and
739 evaporation-transpiration partitioning from a stable isotope survey of lakes in northern
740 Canada. *Global Biochem. Cycles*, **16**, 1026, doi:10.1029/2001Gb001839.

741 Goldsmith, G. R., L. E. Munoz-Villers, F. Holwerda, J. J. McDonnell, H. Asbjornsen,
742 and T. E. Dawson, 2012: Stable isotopes reveal linkages among ecohydrological
743 processes in a seasonally dry tropical montane cloud forest. *Ecohydrol.*, **5**, 779–790,
744 <https://doi.org/10.1002/eco.268>.

745 Good, S. P., D. Noone, and G. Bowen, 2015: Hydrologic connectivity constrains
746 partitioning of global terrestrial water fluxes. *Science*, **349**, 175–177.

747 Hayashi, M., W. L. Quinton, A. Pietroniro, and J. J. Gibson, 2004: Hydrologic functions
748 of wetlands in a discontinuous permafrost basin indicated by isotopic and chemical
749 signatures. *J. Hydrol.*, **296**, 81–97.

750 Hewlett, J. D., and A. R. Hibbert, 1967: Forest Hydrology (eds. Sopper W E & Lull H
751 W) .Pergamon, 275–291.

752 Horton, J. H., and R. H. Hawkins, 1965: Flow path of rain from soil surface to water
753 table. *Soil Sci.*, **100**, 377–383.

754 Hrachowitz, M., H. Savenije, T. A. Bogaard, D. Tetzlaff, and C. Soulsby, 2013: What
755 can flux tracking teach us about water age distribution patterns and their temporal
756 dynamics?. *Hydrol. Earth Syst. Sci.*, **17**, 533–564, [https://doi.org/10.5194/hess-17-533-](https://doi.org/10.5194/hess-17-533-2013)
757 [2013](https://doi.org/10.5194/hess-17-533-2013).

758 Hrachowitz, M., P. Benettin, B. M. van Breukelen, O. Fovet, N. J. K. Howden, L. Ruiz,
759 Y. van der Velde, and A. J. Wade, 2016: Transit times-the link between hydrology and
760 water quality at the catchment scale. *Wiley Interdiscip. Rev.: Water*, **3**, 629–657,
761 <https://doi.org/10.1002/wat2.1155>.

762 Hu, H., F. Dominguez, P. Kumar, J. McDonnell, and D. Gochis, 2018: A numerical
763 water tracer model for understanding event-scale hydrometeorological phenomena *J.*
764 *Hydrometeor.*, **19**, 947–967.

765 Iijima, Y., T. Nakamura, H. Park, Y. Tachibana, and A. N. Fedorov, 2016:
766 Enhancement of Arctic storm activity in relation to permafrost degradation in eastern
767 Siberia. *Int. J. Climatol.*, **36**, 4265–4275, <https://doi.org/10.1002/joc.4629>.

768 Jackson R. B., J. Canadell, J. R. Ehleringer, H. A. Mooney, O. E. Sala, and E. D.
769 Schulze, 1996: A global analysis of root distributions for terrestrial biomes. *Oecologia*,
770 **108**, 389–411.

771 Jasechko, S., Z. D. Sharp, J. J. Gibson, S. J. Birks, Y. Yi, and P. J. Fawcett, 2013:
772 Terrestrial water fluxes dominated by transpiration. *Nature*, **496**, 347–350.

773 Jasechko, S., J. W. Kirchner, J. M. Welker, and J. J. McDonnell, 2016: Substantial
774 proportion of global streamflow less than three months old. *Nat. Geosci.*, **9**, 126–129,
775 <https://doi.org/10.1038/ngeo2636>.

776 Kim, Y., J. S. Kimball, D. A. Robinson, and C. Derksen, 2015: New satellite climate
777 data records indicate strong coupling between recent frozen season changes and snow
778 cover over high northern latitudes. *Environ. Res. Lett.*, **10**, 084004, doi:10.1088/1748-
779 9326/10/8/084004.

780 Kotani, A., A. Saito, A. V. Kononov, R. E. Petrov, T. C. Maximov, Y. Iijima, and T.
781 Ohta, 2019: Impact of unusually wet permafrost soil on understory vegetation and CO₂
782 exchange in a larch forest in eastern Siberia. *Agric. For. Meteorol.*, **265**, 295–309,
783 <https://doi.org/10.1016/j.agrformet.2018.11.025>.

784 Kurita, N., A. Sugimoto, Y. Fujii, T. Fukazawa, V. N. Makarov, O. Watanabe et al.,
785 2005: Isotopic composition and origin of snow over Siberia. *J. Geophys. Res.*, **110**,
786 D13102, <https://doi.org/10.1029/2004JD005053>.

787 Lachniet, M. S., D. E. Lawson, H. Stephen, A. R. Sloat, and W. P. Patterson, 2016:
788 Isoscapes of δ¹⁸O and δ²H reveal climatic forcings on Alaska and Yukon precipitation.
789 *Water Resour. Res.*, **52**, 6575–6586, <https://doi.org/10.1002/2016WR019436>.

790 Majoube, M., 1971: Oxygen-18 and deuterium fractionation between water and steam
791 (in French). *J. Chim. Phys. Phys-Chim. Biol.*, **68**, 1423–1436.

792 McGuire, K. J., J. J. McDonnell, M. Weiler, C. Kendall, B. L. McGlynn, J. M. Welker,
793 and J. Seibert, 2005: The role of topography on catchment-scale water residence time.
794 *Water Resour. Res.*, **41**, <https://doi.org/10.1029/2004WR003657>.

795 McDonnell, J. J., 1990: A rationale for old water discharge through macropores in a
796 steep, humid catchment. *Water Resour. Res.*, **26**, 2821–2832,
797 <https://doi.org/10.1029/WR026i011p02821>.

798 Merlivat, L., L. Jouzel, 1979: Global climatic interpretation of the deuterium oxygen 18
799 relationship for precipitation. *J. Geophys. Res.*, **84**, 5029–5033.

800 Miyazaki, S., K. Saito. *et al.*, 2015: The GRENE-TEA model intercomparison project
801 (GTMIP): Overview and experiment protocol for stage 1. *Geosci. Model Develop.*, **8**,
802 2841–2856, <https://doi.org/10.5194/gmd-8-2841-2015>.

803 Nepstad, D. C., C. R. de Carvalho, E. A. Davidson, P. H. Jipp, P. A. Lefebvre, G. H.
804 Negrelros, E. D. da Silva, T. A. Stone, S. E. Trumbore, and S. Vielra, 1994: The role of
805 deep roots in the hydrological and carbon cycles of Amazonian forests and pastures.
806 *Nature*, **372**, 666–669.

807 Ohta, T., A. Kotani, Y. Iijima, T. C. Maximov, S. Ito, M. Hanamura, A. V. Kononov,
808 and A. P. Maximov, 2014: Effects of waterlogging on water and carbon dioxide fluxes

809 and environmental variables in a Siberian larch forest, 1998–2011. *Agric. For.*
810 *Meteorol.*, **188**, 64–75, <https://doi.org/10.1016/j.agrformet.2013.12.012>.

811 Oleson, K. W., D. M. Lawrence, G. B. Bonan, M. G. Flanner, E. Kluzek, P. J.
812 Lawrence, et al., 2010: Technical description of version 4.0 of the community land
813 model (CLM). NCAR technical note, NCAR/TN-478+STR, pp 257.

814 Park, H., T. Yamazaki, K. Yamamoto, and T. Ohta, 2008: Tempo-spatial characteristics
815 of energy budget and evapotranspiration in the eastern Siberia. *Agric. For. Meteorol.*,
816 **148**, 1990–2005, <https://doi.org/10.1016/j.agrformet.2008.06.018>.

817 Park, H., Y. Iijima, H. Yabuki, T. Ohta, J. Walsh, Y. Kodama, and T. Ohata, 2011: The
818 application of a coupled hydrological and biogeochemical model (CHANGE) for
819 modeling of energy, water, and CO₂ exchanges over a larch forest in eastern Siberia. *J.*
820 *Geophys. Res.*, **116**, D15102, doi:10.1029/2010JD015386.

821 Park, H., A. N. Fedorov, M. N. Zheleznyak, P. Y. Konstantinov, and J. E. Walsh, Effect
822 of snow cover on pan-Arctic permafrost thermal regimes. *Clim. Dyn.*, **44**, 2873–2895.

823 Park, H., Y. Kim, and J. S. Kimball, 2016: Widespread permafrost vulnerability and soil
824 active layer increases over the high northern latitudes inferred from satellite remote
825 sensing and process model assessments. *Remote Sens. Environ.*, **175**, 349–358,
826 <https://doi.org/10.1016/j.rse.2015.12.046>.

827 Park, H., S. Launiainen, P. Y. Konstantinov, Y. Iijima, and A. N. Fedorov, 2018:
828 Modeling the effect of moss cover on soil temperature and carbon fluxes at a tundra site
829 in Northeastern Siberia. *J. Geophys. Res.-Biogeosci.*, **123**,
830 <https://doi.org/10.1029/2018JG004491>.

831 Risi, C., and Coauthors, 2016: The water isotopic version of the land-surface model
832 ORCHIDEE: Implementation, evaluation, sensitivity to hydrological parameters.
833 *Hydrol. Curr. Res.*, **7**, 258, doi: [10.4172/2157-7587.1000258](https://doi.org/10.4172/2157-7587.1000258).

834 Serreze, M. C., D. H. Bromwich, M. P. Clark, A. J. Etringer, T. Zhang, and R.
835 Lammers, 2002: Large-scale hydro-climatology of the terrestrial Arctic drainage
836 system. *J. Geophys. Res.*, **107**, 8160, <https://doi.org/10.1029/2001JD000919>.

837 Sturm, C., Q. Zhang, and D. Noone, 2010: An introduction to stable water isotopes in
838 climate models: Benefits of forward proxy modelling for paleoclimatology. *Climate*
839 *Past*, **6**, 115–129, <https://doi.org/10.5194/cp-6-115-2010>.

840 Sugimoto, A., D. Naito, N. Yanagisawa, K. Ichiyangi, N. Kurita, J. Kubota, T. Kotake,
841 T. Ohata, T. C. Maximov, and A. N. Fedorov, 2003: Characteristics of soil moisture in
842 permafrost observed in East Siberian taiga with stable isotopes of water. *Hydrol.*
843 *Process.*, **17**, 1073–1092, <https://doi.org/10.1002/hyp.1180>.

844 Tan, A., J. C. Adam, and D. P. Lattenmaier, 2011: Change in spring snowmelt timing in
845 Eurasian Arctic rivers. *J. Geophys. Res.*, 116, D3,
846 <https://doi.org/10.1029/2010JD014337>.

847 Ueta, A., A. Sugimoto, Y. Iijima, H. Yabuki, T. C. Maximov, T. A. Velivetskaya, and
848 A. V. Ignatiev, 2013: Factors controlling diurnal variation in the isotopic composition
849 of atmospheric water vapour observed in the taiga, eastern Siberia. *Hydrol. Proc.*, **27**,
850 2295–2305, doi:10.1002/hyp.9361.

851 Vasil'chuk, Y. K., V. Shevchenko, A. Lisitzin, N. Budantseva, S. Vorobiov, S. Kirpotin
852 et al., 2016: Oxygen isotope and deuterium composition of snow cover on the profile of
853 Western Siberia from Tomsk to the Gulf of Ob. *Dokl. Earth Sc.*, **471**, 1284–1287,
854 doi:10.1134/S1028334X1612014X.

855 Welp, L., J. Randerson, J. Finlay, S. Davydov, G. Zimova, A. Davydova, et al., 2005: A
856 high-resolution time series of oxygen isotopes from the Kolyma River: implications for
857 the seasonal dynamics of discharge and basin-scale water use. *Geophys. Res. Lett.*, **32**,
858 L14401, <https://doi.org/10.1029/2005GL022857>.

859 White, M. A., P. E. Thornton, and S. W. Running, 1997: A continental phenology
860 model for monitoring vegetation responses to interannual climatic variability. *Global*
861 *Biogeochem. Cycles*, **11**, 217–234. <https://doi.org/10.1029/97GB00330>.

862 Williams, M., B. E. Law, P. M. Anthoni, and M. Unsworth, 2001: Using a simulation
863 model and ecosystem flux data to examine carbon-water interactions in ponderosa pine.
864 *Tree Physiol.*, **21**, 287–298.

865 Woo, M., D. L. Kane, S. K. Carey, and D. Yang, 2008: Progress in permafrost
866 hydrology in the new millennium. *Permafrost Periglac. Process.*, **19**, 237–254.

867 Yang, D., B. Ye, and A. Shiklomanov, 2004: Discharge characteristics and changes
868 over the Ob river watershed in Siberia. *J. Hydrometeorol.*, **5**, 595–610.

869 Yang, Y., R. J. Donohue, and T. R. McVicar. 2016. Global estimation of effective plant
870 rooting depth: Implications for hydrological modeling, *Water Resour. Res.*, 52, 8260–
871 8276, doi:10.1002/2016WR019392

872 Ye, H., S. Ladochy, D. Yang, T. Zhang, X. Zhang, and M. Ellison, 2004: The impact of
873 climatic conditions on seasonal river discharges in Siberia. *J. Hydrometeorol.*, **5**, 286–
874 295.

875 Yoshimura, K., S. Miyazaki, S. Kanae, and T. Oki, 2006. Iso-MATSIRO, a land surface
876 model that incorporates stable water isotopes. *Global Planet. Change*, **51**, 90–107,
877 <https://doi.org/10.1016/j.gloplacha.2005.12.007>.

887 Yoshimura, K., M. Kanamitsu, D. Noone, and T. Oki, 2008: Historical isotope
888 simulation using Reanalysis atmospheric data. *J. Geophys. Res.*, **113**, D19108,
889 doi:10.1029/2008JD010074.

890 Zhang, K., J. S. Kimball, Q. Mu, L. A. Jones, S. J. Goetz, and S. W. Running, 2010:
891 Satellite based analysis of northern ET trends and associated changes in the regional
892 water balance from 1983 to 2005. *J. Hydrol.*, 379, 92–110,
893 <https://doi.org/10.1016/j.jhydrol.2009.09.047>.

1 **Table 1.** Summary of the separation of snowmelt and rainfall contributions to evapotranspiration and the subcomponents (mm yr⁻¹) in
 2 the three experiments, averaged for the study period (1980–2016). Numbers in parentheses represent individual percentages to the total
 3 of either evapotranspiration or the subcomponents.

4

Exp	<i>ET</i>			<i>E_t</i>			<i>E_i</i>			<i>E_s</i>		
	total	snow	rain	total	snow	rain	total	snow	rain	total	snow	rain
<i>S</i> _{CN}	185.7	37.0 (19.9)	148.7 (80.1)	117.2	16.6 (14.2)	100.6 (85.8)	33.1	13.3 (40.2)	19.8 (59.8)	35.5	7.1 (20.0)	28.4 (80.0)
<i>S</i> _{MT}	189.4	37.6 (19.9)	151.8 (80.1)	120.7	17.3 (14.3)	103.4 (85.7)	33.0	13.2 (40.0)	19.8 (60.0)	35.7	7.1 (19.9)	28.6 (80.1)
<i>S</i> _{AB}	185.9	37.0 (19.9)	148.9 (80.1)	117.3	16.7 (14.29)	100.6 (85.8)	33.1	13.3 (40.2)	19.8 (59.8)	35.5	7.1 (20.0)	28.4 (80.0)
Mea n	187.0	37.2 (19.9)	149.8 (80.1)	118.4	16.9 (14.3)	101.5 (85.7)	33.1	13.3 (40.2)	19.8 (59.8)	35.6	7.1 (19.9)	28.5 (80.1)

5

6

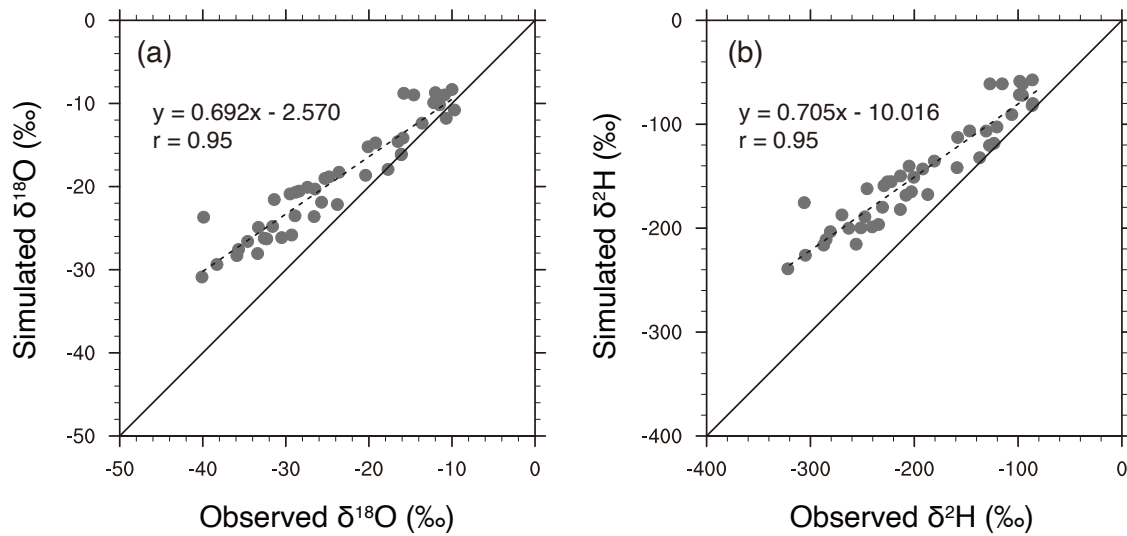


Figure 1. Comparison of IsoGSM-simulated isotope values used for CHANGE simulation to the records observed at Yakutsk station (1996–2000), archived as part of the Global Network of Isotopes in Precipitation by the International Atomic Energy Agency. Overestimated isotope values were adjusted to the observations using a scaling coefficient of 1.3.

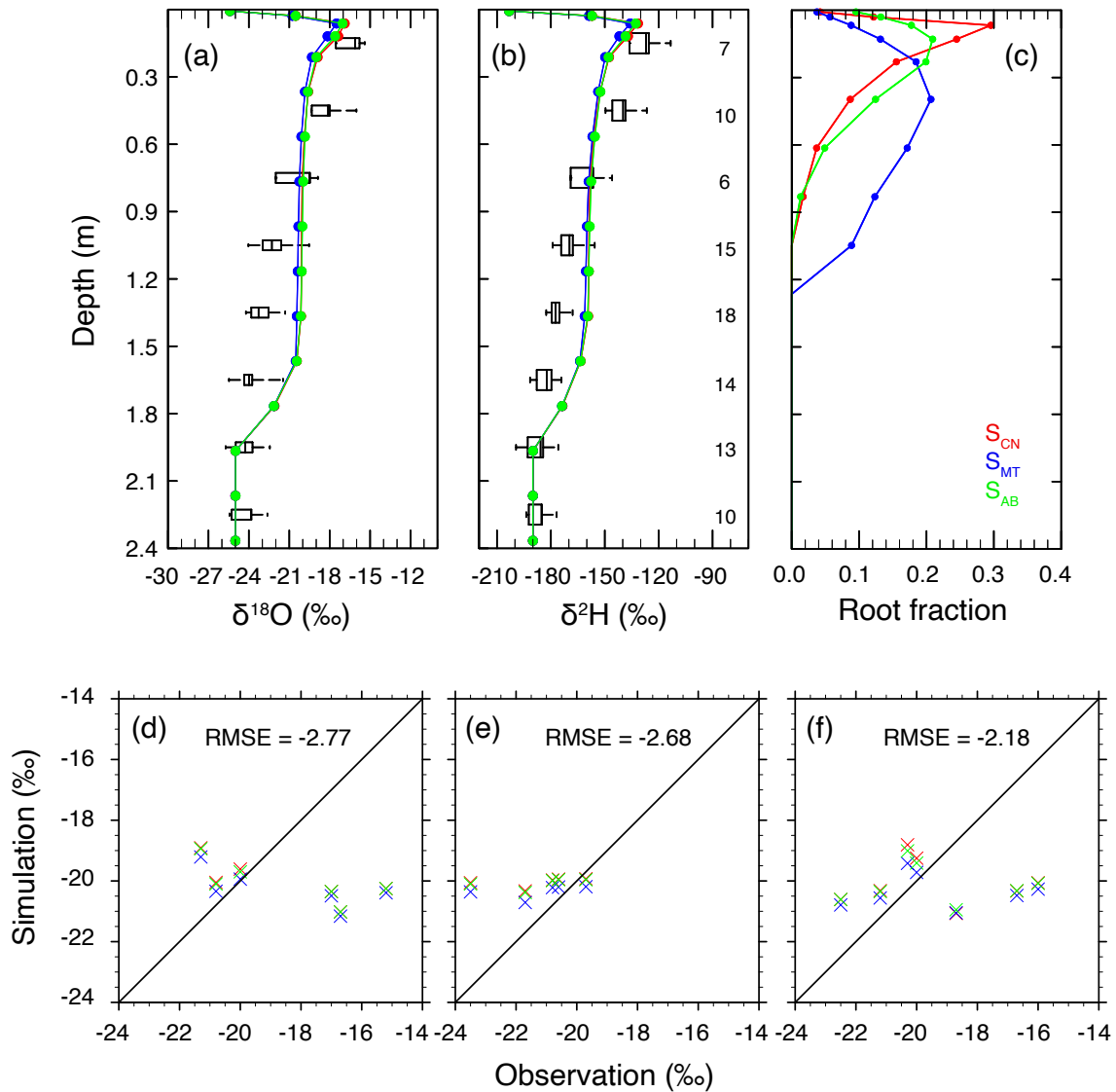


Figure 2. Comparison of (a) oxygen and (b) hydrogen simulated by the three experiments plotted against observations of analyzed soil cores sampled in March 2010. The samples within each 30-cm depth were integrally averaged, showing the distributions as boxplots. Numbers on the right in (b) refer to the sample numbers used for the average. The vertical root profiles of the three experiments are compared in (c). The model-averaged oxygen isotopic ratios of two soil layers, that is, (d) 0–0.3 m and (e) 0.3–0.6 m, and (f) transpiration are compared against the values sampled during the growing seasons of 1998–2000 at the same study site (Sugimoto et al., 2003). Modeled isotope ratios were averaged for 10 days prior to the observation date.

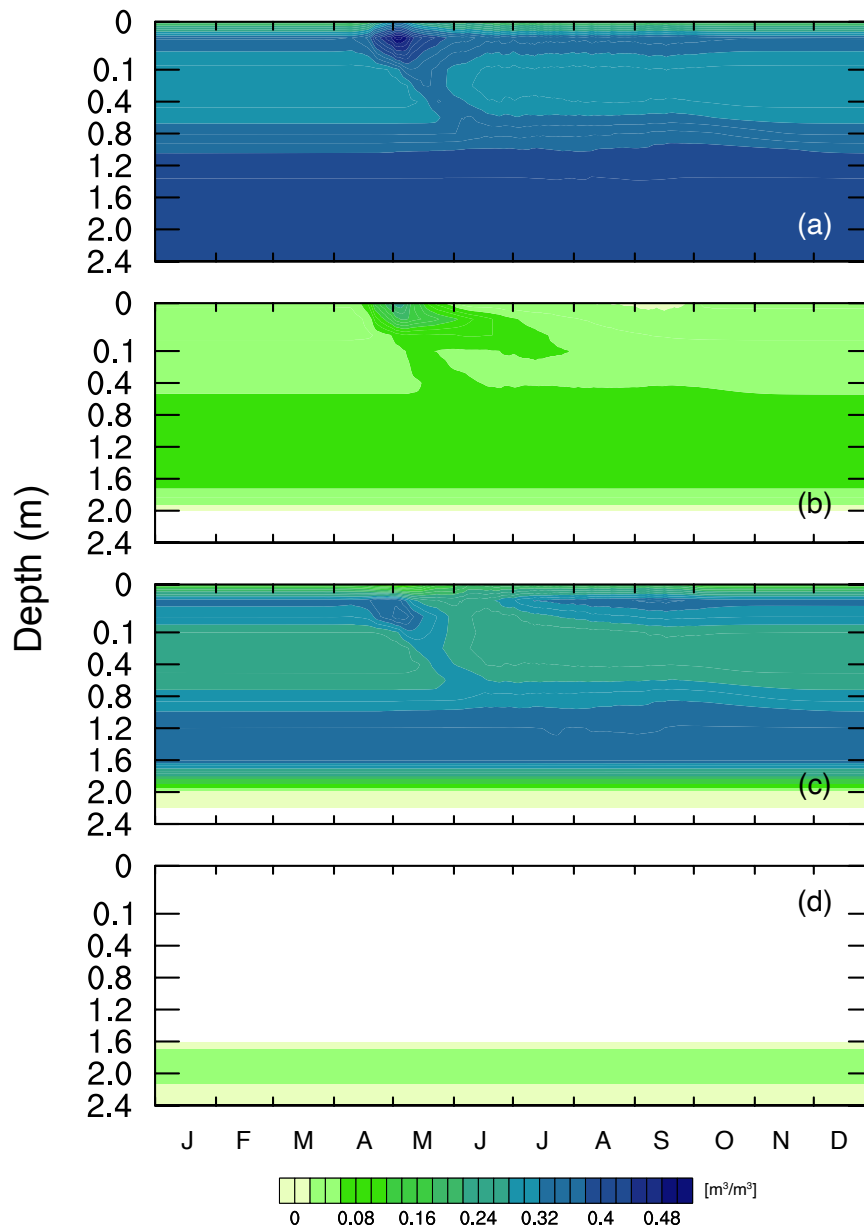


Figure 3. Seasonal variability of the vertical profile of (a) soil moisture and the separated (b) snowmelt, (c) rainfall, and (d) permafrost-originated waters, averaged for each date during 1980–2016 in the case of the control experiment.

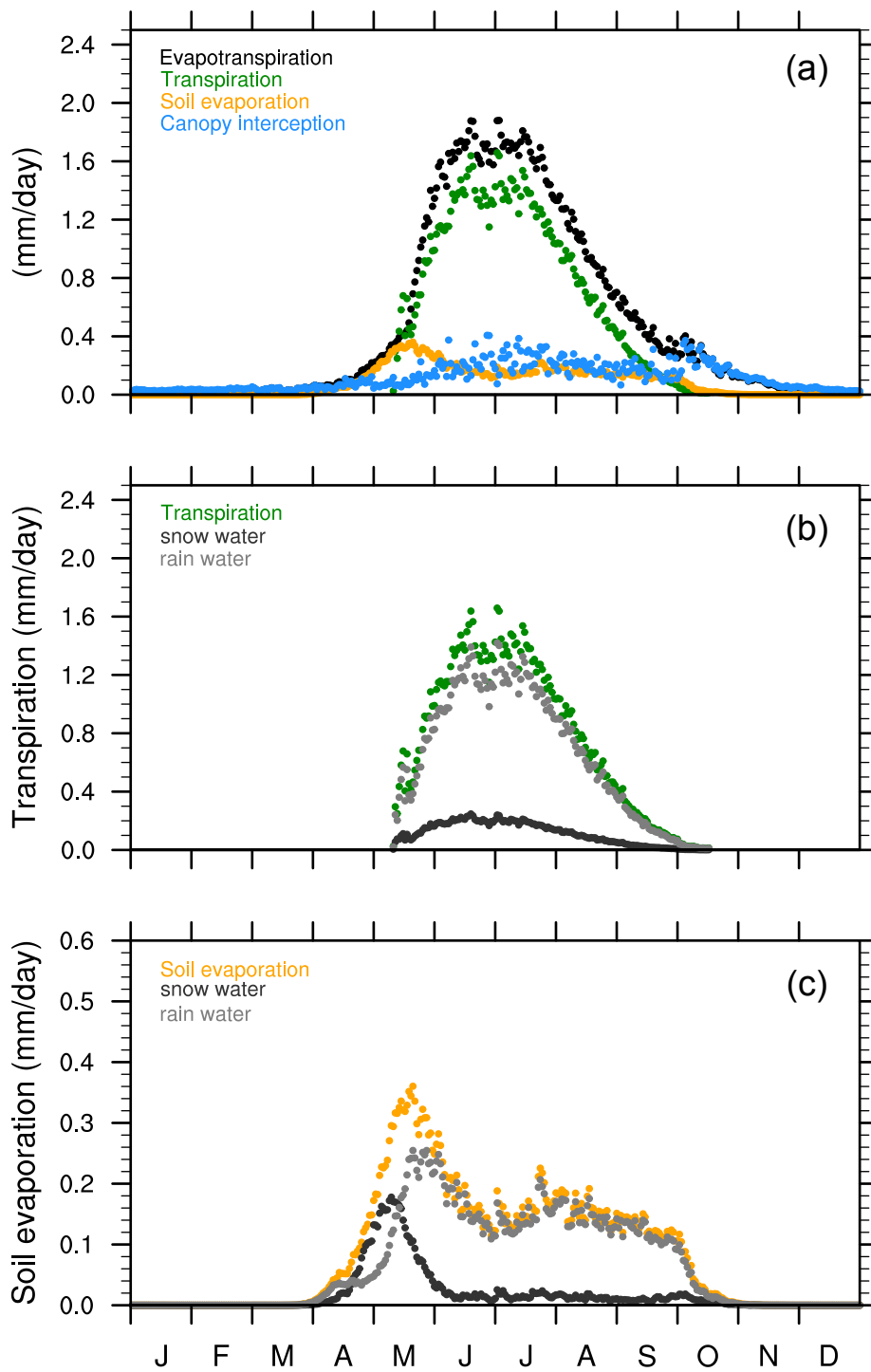


Figure 4. Time series for (a) daily evapotranspiration and the subcomponents averaged for each date during 1980–2016 in the case of the control experiment, and the variation of the contributions of snowfall and rainfall to (b) transpiration and (c) soil evaporation.

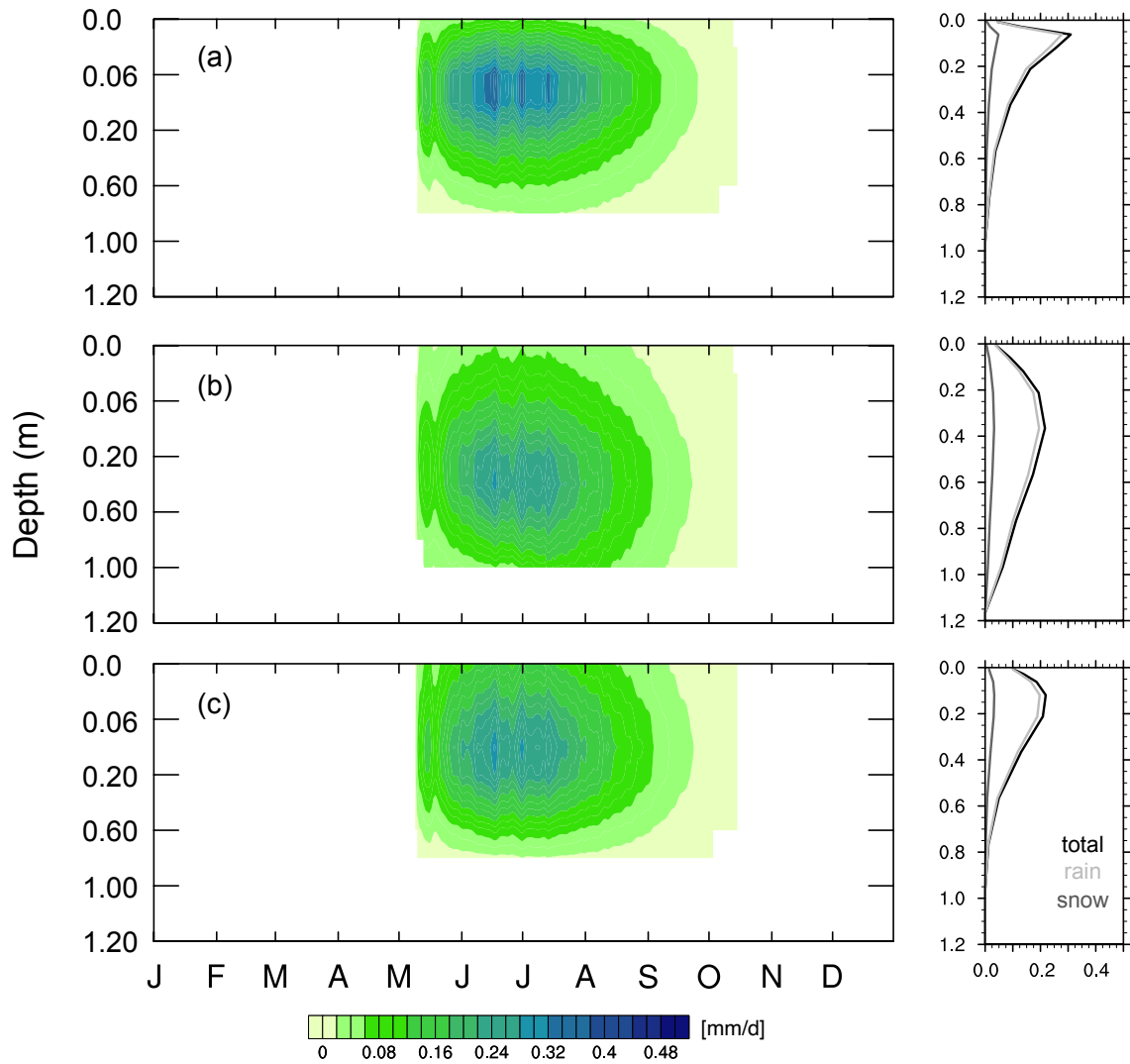


Figure 5. Seasonal variability of vertically distributed transpiration simulated by the three experiments: (a) S_{CN} , (b) S_{MT} , and (c) S_{AB} , averaged for each date during 1980–2016 (left panels), and the associated averaged vertical profiles of rainfall and snowmelt used for transpiration in the individual experiments (right-hand panels).

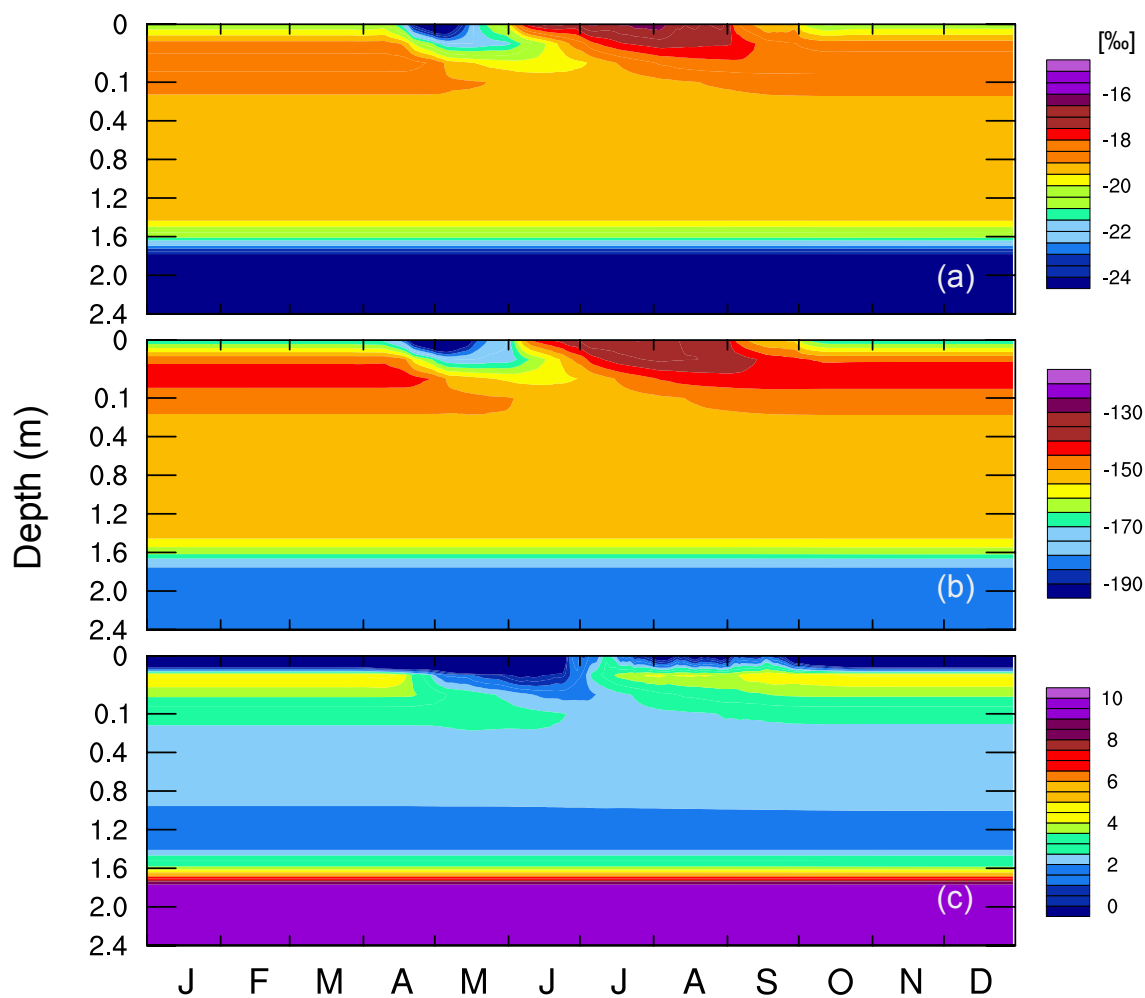


Figure 6. Seasonal variability of vertically distributed daily (a) oxygen, (b) hydrogen, and (c) d-excess isotopes, averaged for each date during 1980–2016 in the case of the control experiment.

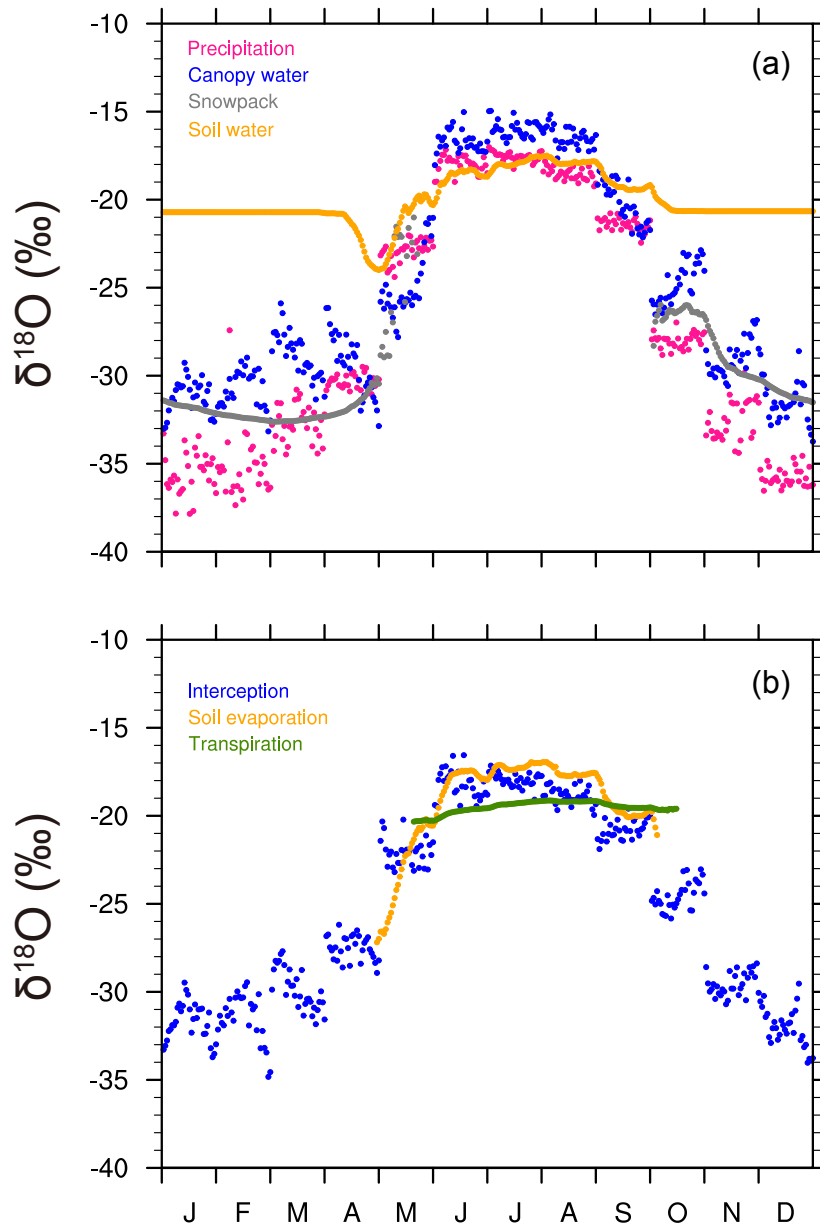


Figure 7. Time series of daily (a) oxygen isotope of precipitation-derived water storages of canopy, snow, and soil, and (b) evaporation from the surfaces and transpiration, averaged for each date during 1980–2016 in the case of the control experiment. The isotope ratio of soil water in (a) was averaged for 0–10-cm soil layers.

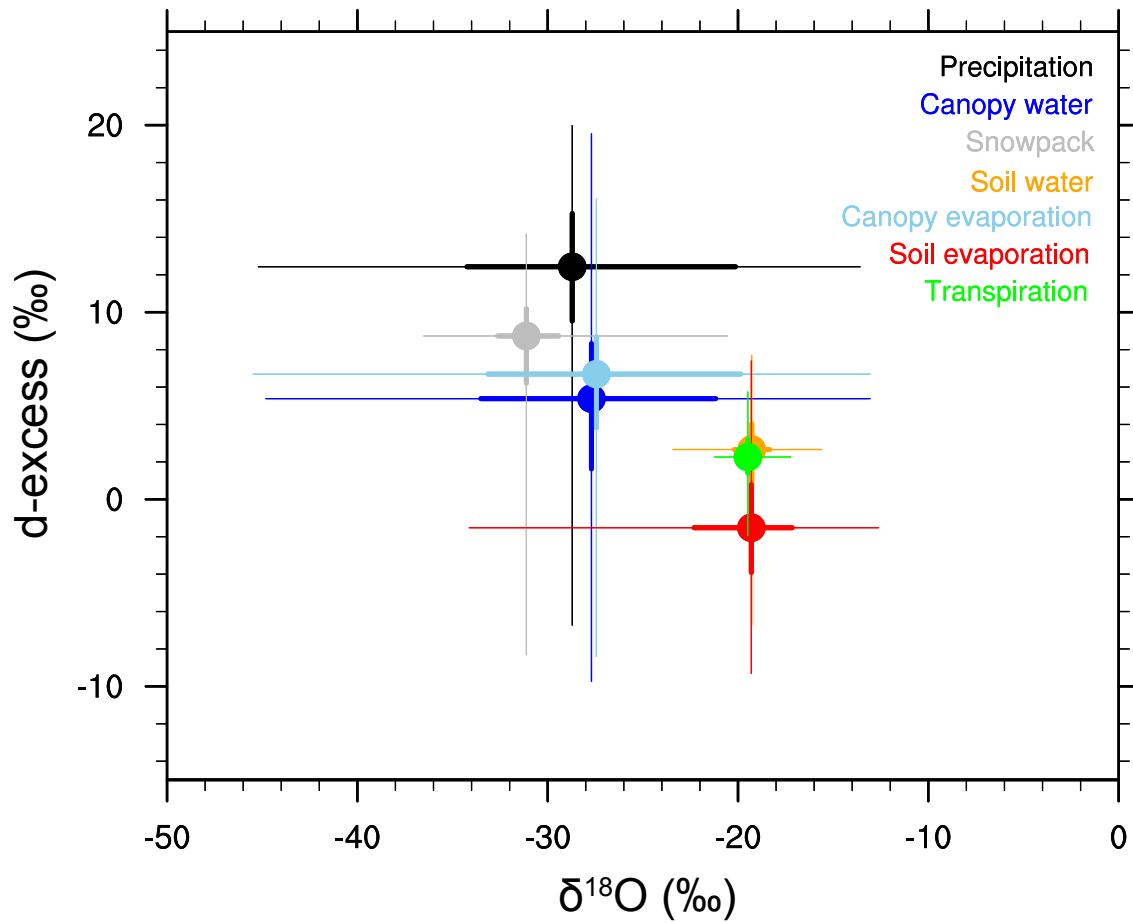


Figure 8. Isotopic plots of oxygen isotope and d-excess grouping precipitation, canopy water, snow, canopy evaporation, soil evaporation, transpiration, and soil water with different colors. The dots indicate medians of the interquartile ranges in boxplots analyzed using monthly averaged values, and the thick lines in the vertical and horizontal directions represent the ranges of the low and high quartiles in the boxplots of individual compositions. The thin lines show the maximum and minimum distribution of the monthly averaged values for the compositions.

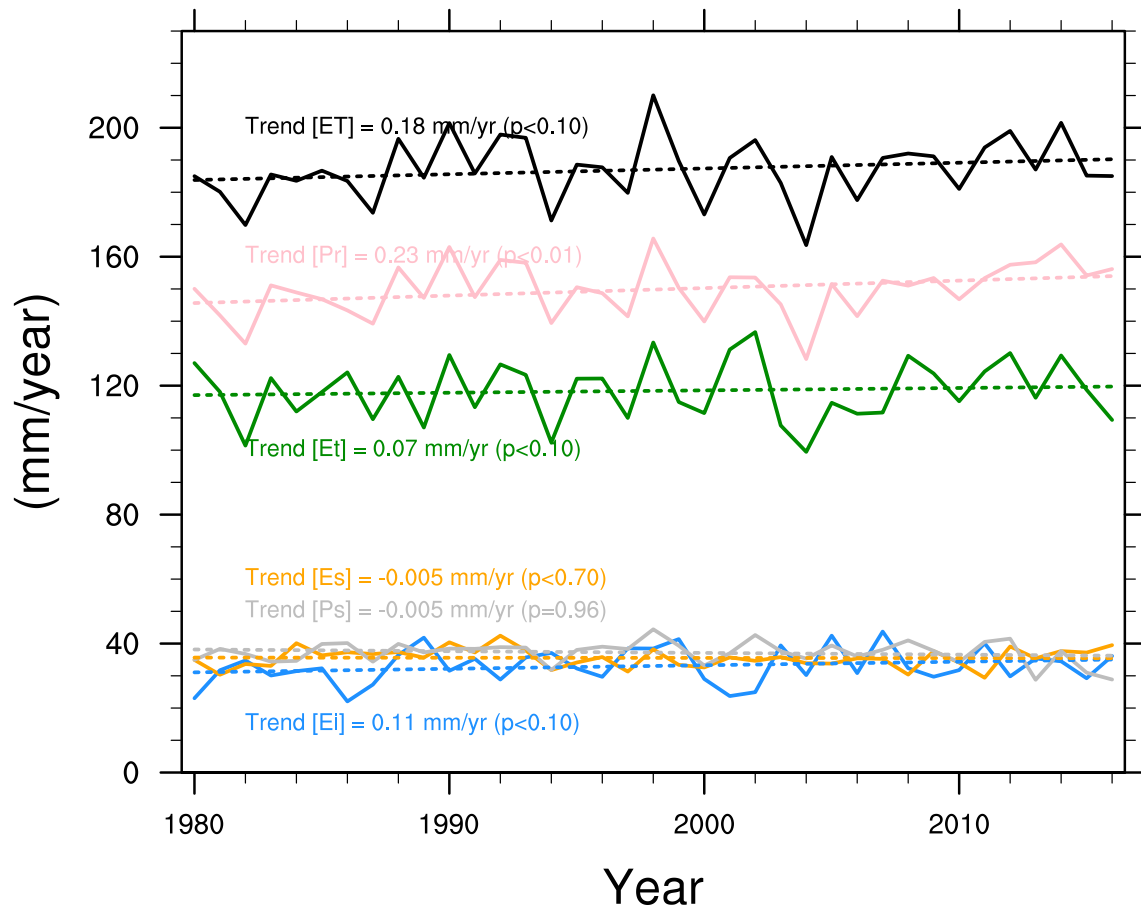


Figure 9. Interannual variability of the simulated evapotranspiration and subcomponents with rainfall (P_r) and snowmelt (P_s) waters used for evapotranspiration. The dotted lines indicate the trend of the individual variables.

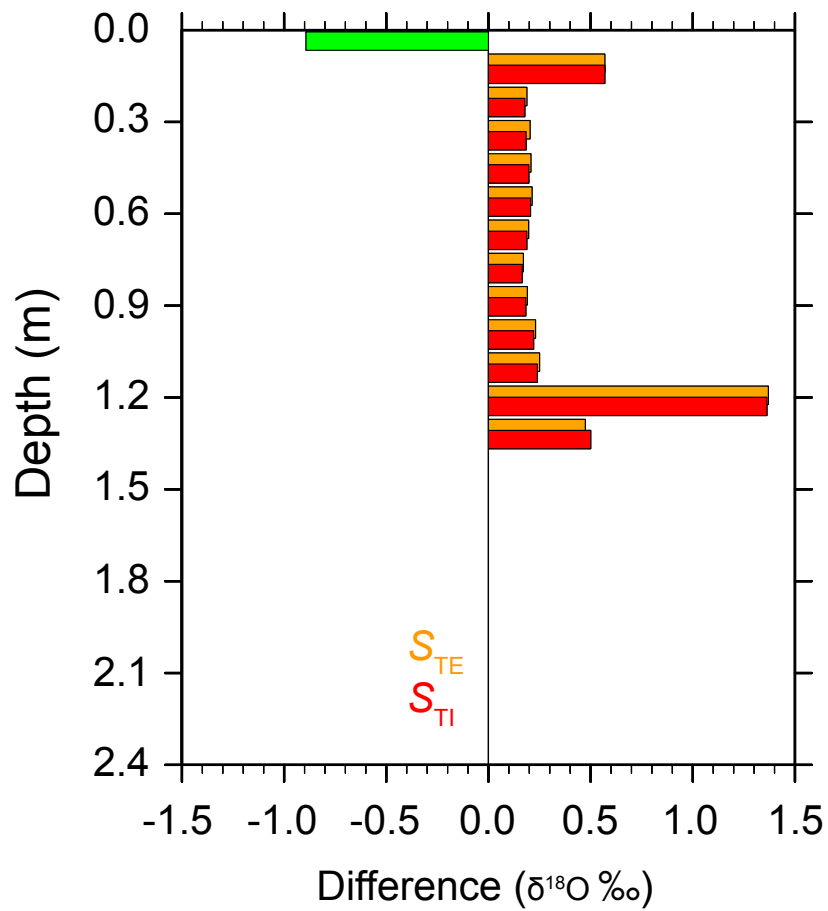


Figure 10. Vertical difference in soil water $\delta^{18}O$ between the sensitivity experiments with root depths extended to 1.56 m and the control experiment in March 2010, when the observational records were used for validation of the simulations. The two sensitivity experiments differed in that the soil freezing stress by permafrost was excluded (S_{TE}) or included (S_{TI}).

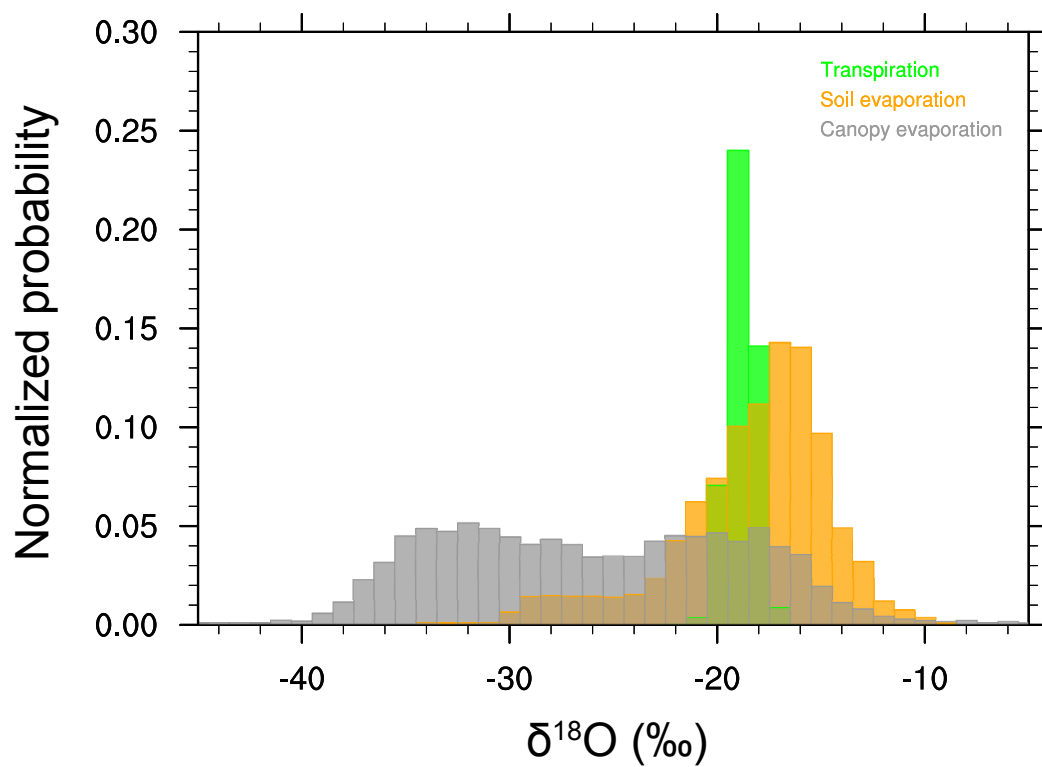


Figure 11. Normalized distribution of the $\delta^{18}\text{O}$ of *ET* components (soil and canopy evaporation and transpiration) during 1980–2016.